https://doi.org/10.15407/ufm.22.04.562

M.O. VASYLYEV[1,*], B.N. MORDYUK[2,1,], S.M. VOLOSHKO[2], and D.A. LESYK[2]**

[1] G.V. Kurdyumov Institute for Metal Physics of the N.A.S. of Ukraine, 36 Academician Vernadsky Blvd., UA-03142 Kyiv, Ukraine

[2] National Technical University of Ukraine 'Igor Sikorsky Kyiv Polytechnic Institute', 37 Peremohy Ave., UA-03056 Kyiv, Ukraine

* vasil@imp.kiev.ua, ** mordyuk@imp.kiev.ua

MICROSTRUCTURE EVOLUTION OF THE CARBON STEELS DURING SURFACE SEVERE PLASTIC DEFORMATION

The review is devoted to the state-of-the-art views on the microstructure evolution in structural and tool carbon steels during the surface severe plastic deformation (SPD). The main focus is on the effects of the nanocrystallization in the near-surface area of the low-carbon steel (C 0.05–0.2%), medium-carbon steel (C 0.35–0.65%), and high-carbon steel (C 1.0–1.5%). It is reviewed the following advanced surface SPD methods for the metal surfaces in recent years: an ultrasonic impact peening (UIP), high-frequency impact peening (HFIP), air blast shot peening (ABSP), surface mechanical attrition treatment (SMAT), and laser shock peening (LSP). Microstructure evolution before and after SPD is studied by an optical microscopy (OM), scanning electron microscopy (SEM), and transmission electron microscopy (TEM). The effects of the SPD parameters on the nanocrystalline modification of such main phase components of the carbon steels as ferrite, pearlite and cementite are analysed. The atomic mechanism of the nanocrystallization is presented. The strain-hardening effect induced by SPD is demonstrated by the data of the near-surface microhardness profiles.

Keywords: carbon steels, mechanical surface treatments, severe plastic deformation, microstructure, nanocrystallization, microhardness.

Citation: M.O. Vasylyev, B.M. Mordyuk, S.M. Voloshko, and D.A. Lesyk, Microstructure Evolution of the Carbon Steels during Surface Severe Plastic Deformation, *Progress in Physics of Metals*, **22**, No. 4: 562–618 (2021)

1. Introduction

The ever-increasing requirements for the reliability and safety, providing an increase in the service lifetime of machines and structures dictate the need for the creation and implementation of new technologies that improve the performance characteristics of metals at all stages of the product life cycle. Currently, carbon steels are still the most important structural and tool materials for numerous applications in modern mechanical engineering [1, 2]. Due to the increasing intensity of loading machines with a simultaneous tendency to reduce their weight and with the high requirements for the steel properties, the enhancement in the operational reliability and durability of industrial products, and increasing the efficiency of the machinery and equipment is one of the most important tasks of modern mechanical engineering and other branches of the metalworking industry. For example, for several decades, the automotive industry has been one of the most important markets for steel companies. The global demand of automotive steels is currently estimated at around 90 million tons, which is approximately 13% of the total global market share. Recently, the use of high-strength steels for automotive applications has been dramatically increased not only to enhance the safety and durability of vehicles but also to lighten the vehicle's weight for improving fuel efficiency. To fulfil the increased demands, steel companies have focused on the development of high-strength steels. Carbon steels remain the important materials like railways, bridges, pipelines, and other responsible constructions, where steel products and structures still are the main constituents. Therefore, the prolongation of the operation life of the steel constructions by prevention their degradation under cyclic loading and/or in extremely corrosive environments still is a timely and important task [3].

The performance of machines is directly related to the quality of the surface layer of the parts, and it largely determines their service life. Therefore, engineering practice, particularly the engineering, automotive, and aerospace industries, is currently hard to imagine without finish mechanical surface treatment processes. Finishing surface treatment processes are necessary in order to improve tribological properties, prevent fatigue failures and corrosive destruction of the machine components and parts made of steel. Tribological, fatigue performance, and resistance to the corrosion of the machine components are often enhanced by various kinds of surface modification techniques. In steels, for instance, surface modification can take the form of mechanical properties enhancement (mainly surface hardening) through surface chemical changes such as carburizing, nitriding, *etc*. In some cases, surface hardening can be achieved without a chemical modification, either by thermal treatment, such as thermal hardening, or by mechanical treat-

ment. Surface hardening can be also achieved by the deposition of a distinctive surface layer (coating) of harder material such TiN, CrN, DLC, *etc*. Coatings are usually deposited by a variety of processes, such as chemical vapour deposition (CVD), physical vapour deposition (PVD), thermal spray, *etc*. Therefore, improving the surface layer properties has become a topic that has attracted considerable interest.

Extensive investigations on bulk nanostructured metals have indicated that reducing grain sizes to the nanometer scale by severe plastic deformation (SPD) processes leads to substantial metal hardening. Nanocrystallization of the bulk structural materials has been drawn a lot of attention since nanocrystalline (NC) materials (grain size smaller than 100 nm) have superior mechanical and physical properties to those of the coarse-grained counterparts [3, 4]. It is well known that the strength of the material at low/ambient temperatures is generally described by Hall–Petch (H-P) relationship as follows [5]:

$$\sigma_y = \sigma_0 + k_y/d^{1/2},$$

where σ_y is the yield stress, σ_0 is the material constant required for the starting of dislocation movement, k_y is the strengthening coefficient, and d is the average grain size. The strength and hardness increase monotonically with decreasing grain size according to the empirical Hall–Petch relationship. In addition, the nanostructured layer in the near-surface material may restrain both the initiation and the growth of cracks that increase the fatigue strength.

Optimizing the surface microstructures and properties is the promising way to enhance the overall performance of the materials, including carbon steels. Given the evidence of unique/specific properties for the bulk nanocrystalline materials, it is reasonable to achieve surface modification to improve significantly the overall properties and behaviour of the materials by the generation of the nanostructured surface layer using SPD. Such surface nanocrystallization will provide a new approach to the application of nanotechnology in engineering steels. There are several variants of methods to introduce nanograins and grain size gradients into the near-surface region of bulk metals and alloys based on the principle of the surface severe plastic deformation. The advanced SPD methods of the metal surfaces in recent years are laser shock peening (LSP), air blast shot peening (ABSP or SP), surface mechanical attrition treatment (SMAT), high-frequency (HF) and ultrasonic impact peening (UIP) [6–11]

This review aims to describe the modern views of the nanostructuring processes of the subsurface layers in the low-, medium-, and high-carbon steels under surface severe plastic deformation (SPD).

To analyse the literature data for each of the SPD methods, chronological order is kept up.

2. Severe Surface Deformation by Vibration Impact Peening

2.1. Ultrasonic Impact Peening

In the work [12], the microstructure changes in the surface layer of the cylindrical samples of steel 60 induced by the hard contact of the ultrasonic striker with the tungsten carbide brazing were studied. The chemical composition this steel is next (wt.%): 0.57–0.65 C; 0.60–0.90 Mn; 0.15 V; 0.022–0.45 Si; ≤0.035 P; ≤0.040 S; balance Fe. For ultrasonic processing, a lathe and an ultrasound machine were used. The pressing force of the ultrasonic striker (WC0 was 150 N at the feed rate of 0.07 mm/rev.

The metallographic SEM-cross section image of the microstructure of the processed sample and the layer-by-layer distribution of the microhardness are shown in Figs. 1 and 2, respectively. The microstructure at a depth of 3–45 μm is characterized by the presence of the non-equiaxial grains elongated in the deformation direction. As seen from Fig. 2, the microhardness decreases with depth and reaches the bulk value at the depth of about 400 μm.

More detailed information on changes in the microstructure was obtained using TEM (Fig. 3). In the bulk of the ferrite–pearlite steel sample, the microstructure is a mixture of the lamellar pearlite colonies and ferrite grains. In the ferrite part of pearlite colonies, the presence of the reticular or chaotic component of the dislocation substructure can be observed. Figure 4 demonstrates the formation of the nanocrystalline structure as a result of the ultrasonic treatment at the depth of 2–3 μm. The latter consists of the mixture of α-phase crystallites (35–40 nm) and randomly distributed round cementite particles 15–20 nm in size ([13]; Fe_3C reflections in Fig. 5, *c*). In these areas, the circular structure of the microelectronograms is visible, which indicates the

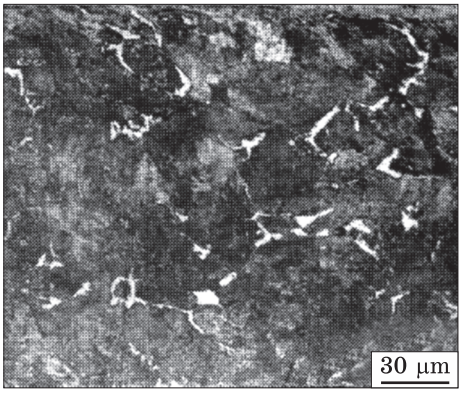

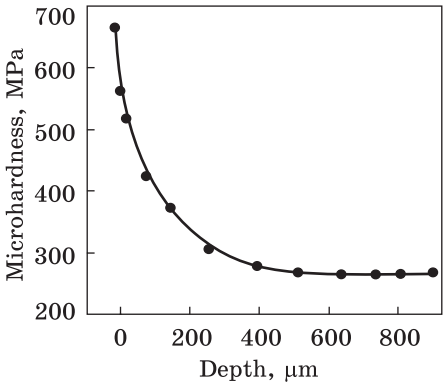

Fig. 1. Cross-section image of the steel 60 microstructure after USFT-treatment [12]

Fig. 2. Layer-by-layer distribution of the microhardness after USFT-treatment [12]

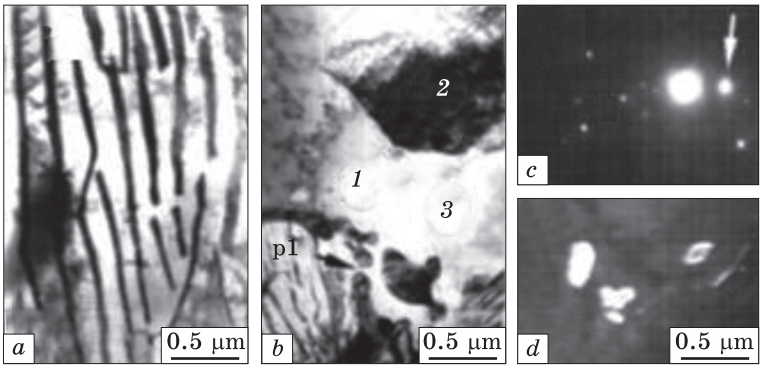

Fig. 3. The initial TEM-microstructure of the steel 60: *a*, *b* — bright field image; *c* — dark field for reflex [8] Fe_3C; *c* — microelectronogram for photo *b*. Numbers refer to ferrite grains; p1 — of the globular perlite grains; the arrow indicates the reflex of the dark field [12]

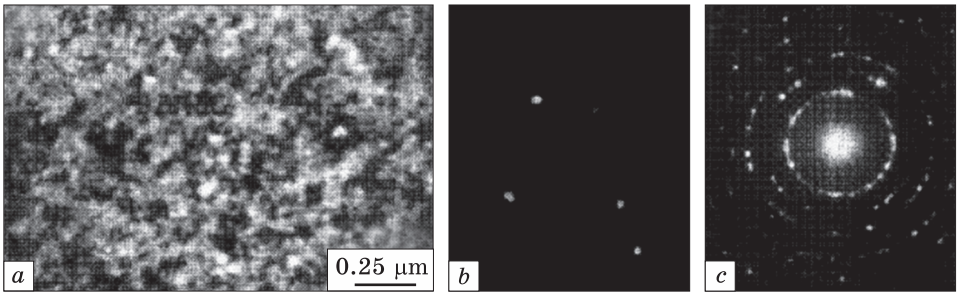

Fig. 4. TEM image of the steel 60 surface after USFT- treatment [12]

high-angle misorientation of the α-phase nanocrystals. The regions of the initial free ferrite are not observed in this case. The formation of this nanostructure is associated, first of all, with deformation fracture of the initial pearlite grains, and, second, with the formation of Cottrell atmospheres around dislocations and the segregation of the carbon atoms at the subboundaries after the destruction of the cementite. Due to the diffusion of the carbon atoms by moving dislocations and dislocation tubes, re-precipitation of the cementite nanoparticles is possible. Noticeable structural changes are observed at the greater depths (3–10 μm). Here, deformation changes are due to fragmentation of the ferrite and cementite plates in the lamellar pearlite (Fig. 5, *a*, *b*). As a result of deformation in the original ferrite, sub-grains with a size of 0.20–0.50 μm are formed (Fig. 5, *d*–*f*).

Authors [14] investigated the tool steel SKD61, the chemical composition of which is given to be the following (wt.%): 0.35–0.42 C; 0.25–0.30 Mn; 0.02 P; 0.02 S; 0.80–1.20 Si; 4.80–5.50 Cr; 0.80–1.15 V; 1.00–1.50 Mo; balance Fe. Ultrasonic processing (USP) was carried out

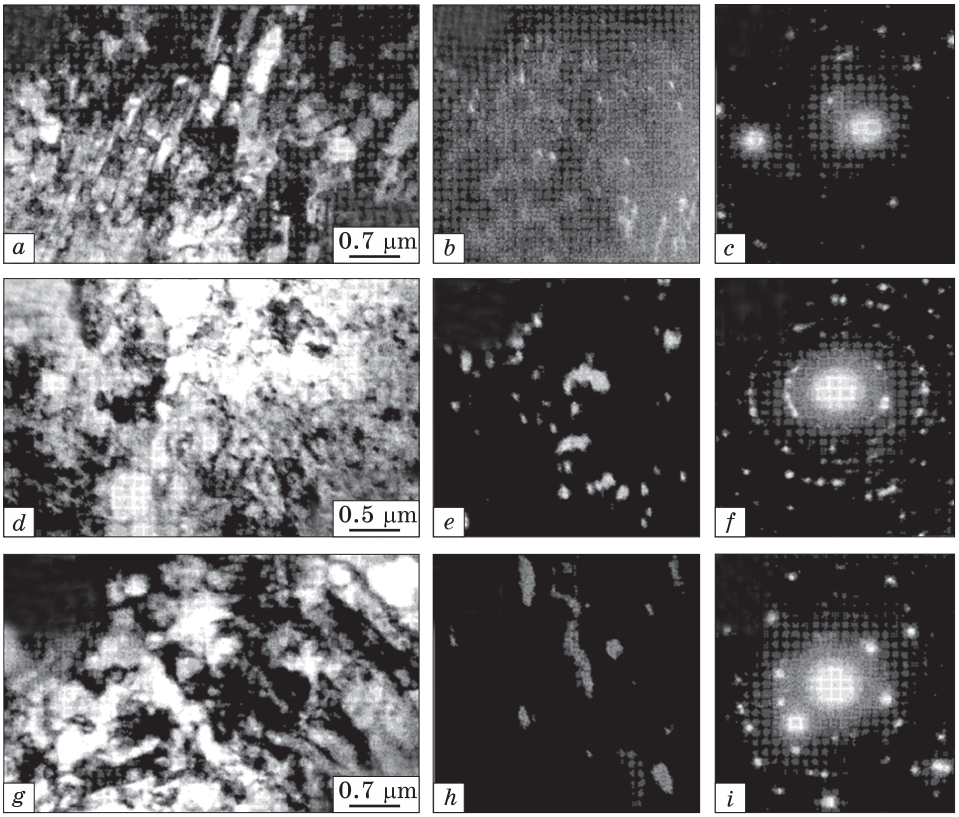

Fig. 5. TEM image of the steel 60 at the depth of 3–4 μm: *a*, *d*, *g* — bright field image; *b* — dark field for reflex [121] Fe_3C; *e* — dark field for reflexes [011] α-Fe^+[201] Fe_3C; *h* — dark field for reflexes [011] α-Fe^+[031] Fe_3C; *c*, *f*, *i* — microelectronograms for photo *a*, *d*, *g*, respectively. Steel structure at depth: ~3 μm (*a*, *f*); ~5 μm (*g*, *i*) [12]

in the mode of hard contact of the tungsten carbide striker with a force of 100 N and the generator frequency of 20 kHz. Figure 6 demonstrates the SEM data showing the structural changes in the surface layers by comparing the samples before (*a*) and after treatment (*b*). In the initial state, microscopic grains are uniformly distributed, while as a result of severe deformation, a near-surface region with the nanoscale grains (*c*) is formed at a depth of up to 100 μm. Transmission electron microscope (TEM) images of the fine microstructure are shown in Fig. 6, *c*. As a rule, before ultrasonic deformation, carbide particles are formed in the form of microplates. However, after processing, this phase is distributed with the average grain size of 50 nm with a not very clear boundary with ferrite grains. The electron diffraction pattern shown in the upper left corner of Fig. 6, *c*, demonstrates the existence of the mixed microstructure consisting of the amorphous and nanocrystalline phases.

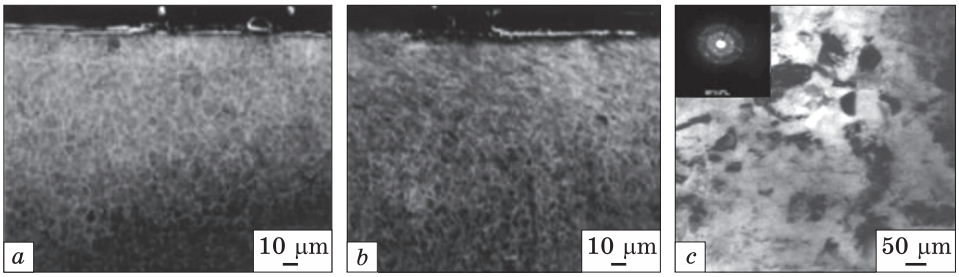

Fig. 6. SEM microstructure of the SKD-61steel: *a* — before and *b* — after USP; *c* — surface layers after USP observed by TEM [14]

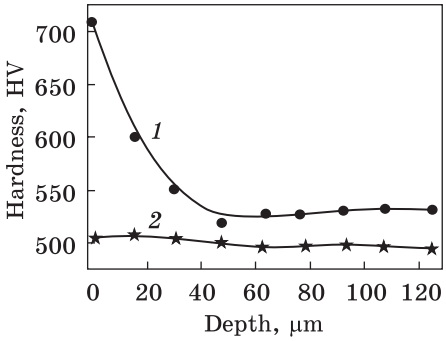

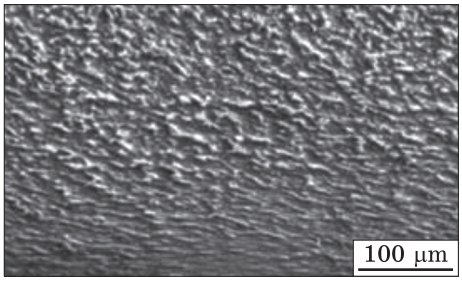

Fig. 7. Layer-by-layer distribution of the microhardness for after (*1*) and before (*2*) by the USP [14]

Fig. 8. Cross-section SEM micrograph of the US-treated specimen [15]

According to the authors of [9], this factor is the main reason for the increased hardness and fatigue strength (Fig. 2 and Fig. 7). Microhardness after processing increases by 37% to a depth of ~60 microns.

In [15], a medium-carbon structural steel of the following chemical composition (wt.%) was investigated: 0.37–0.45 C; 0.80-1.10 Cr; 0.17–0.37 Si; 0.12 Ni; 0.50–0.80 Mn; 0.15 Cu; 0.01 S; balance Fe (steel 40 Cr). Samples in the form of rolls were subjected to ultrasonic treatment after turning, followed by standard quenching and tempering. After such treatment, the structure of the steel consisted of deflected sorbitol and ferrite with a b.c.c. lattice. Ultrasonic processing was carried out at the generator frequency of 20 kHz with a striker/horn amplitude of up to 25 μm. The striker in the form of the rotating tungsten carbide ball was pressed against the sample with the force of 400 N.

The SEM image of the microstructure (Fig. 2) after processing shows a gradient deformed layer up to 150 μm thick. A more detailed analysis of the nanostructured zone formed by deformation was performed using TEM (Fig. 4). The homogeneous layer with equiaxed grains 3–7 nm in size is visible close to the surface. According to electron microdiffrac-

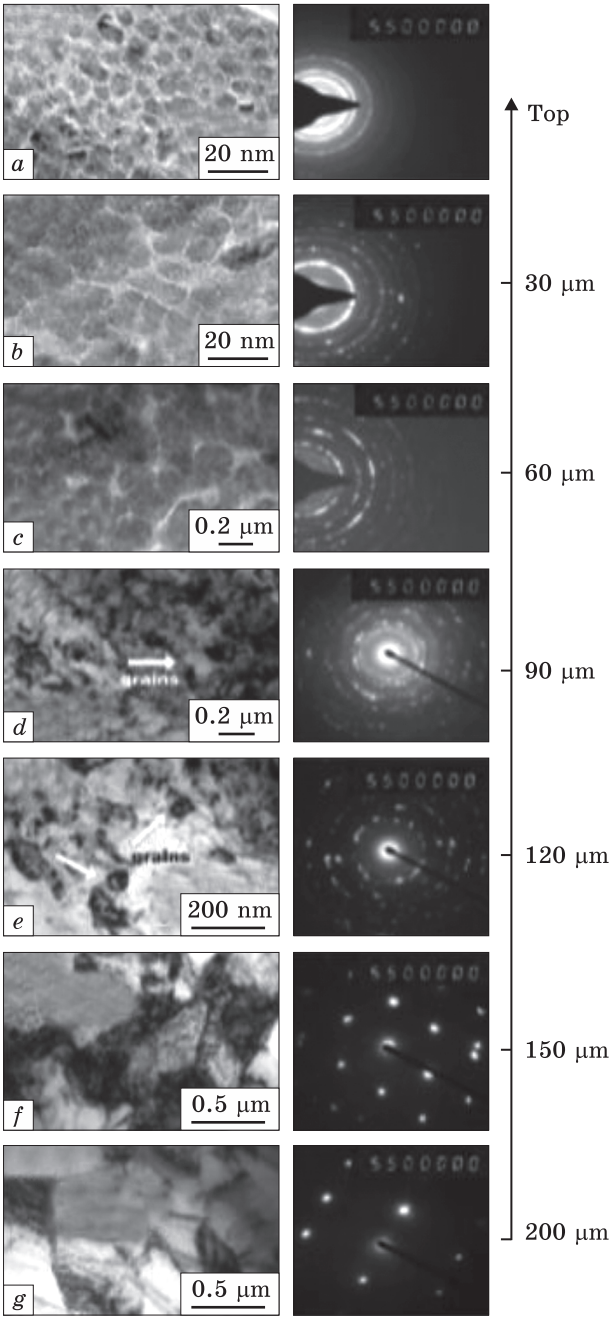

Fig. 9. TEM images and the corresponding selected area electron diffraction patterns (SAED) patterns at different depth of US-treated sample [15]

tion data, the nanoscale grains have a random crystallographic orientation. At the depth of 150 μm, most of the grains are in the form of cells or micrometre-sized blocks. The equiaxed grains 300–500 nm in size with distinct grain boundaries and internal dislocations are observed at an even greater depth (200 μm). The layer-by-layer distribution of the grain size in the deformed layer is shown in Fig. 7.

Comparison of the microhardness distribution along with depth before and after the US treatment can be seen in Fig. 10. The hardening effect is 152%.

A high-carbon structural steel AISI 52100 was investigated by the authors [16]. The steel composition (wt.%): 0.98–1.1 C; 1.3–1.6 Cu; 0.25–0.45 Mn; ≤0.025 P; 0.15–0.3 Si; ≤0.025 S; and balance Fe. Due to its good combination of strength, hardness, and machinability, this steel is mainly used for the manufacture of the bearings, rolls, and vehicle parts.

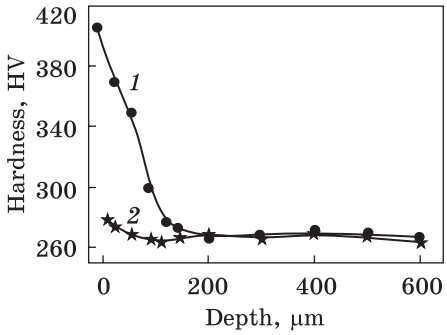

Fig. 10. Comparison of the microhardness depth distribution: After (*1*) and before (*2*) US-treatment [15]

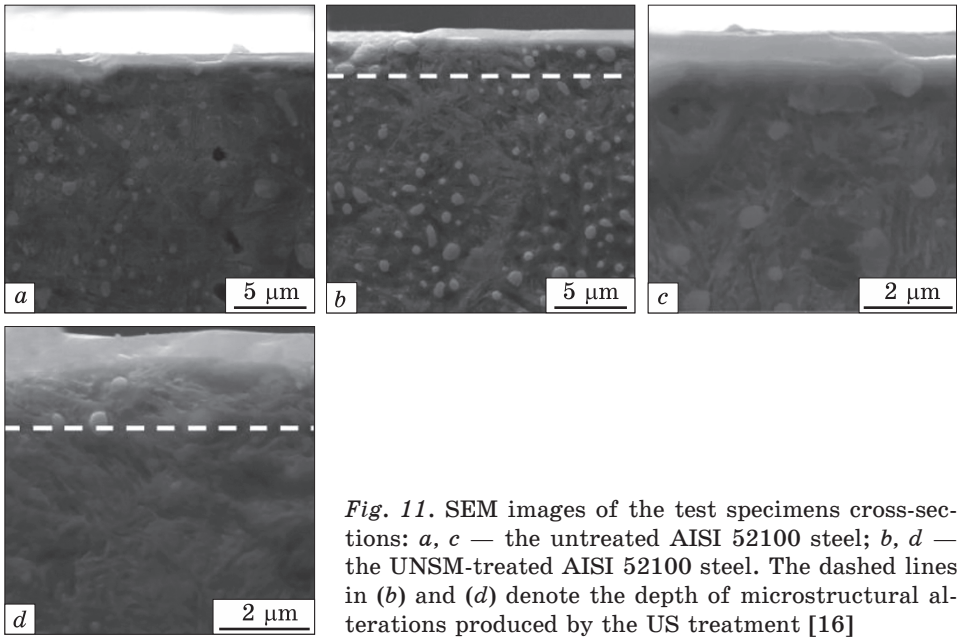

Fig. 11. SEM images of the test specimens cross-sections: *a, c* — the untreated AISI 52100 steel; *b, d* — the UNSM-treated AISI 52100 steel. The dashed lines in (*b*) and (*d*) denote the depth of microstructural alterations produced by the US treatment [16]

For the ultrasonic treatment, the steel discs hardened to 58 HRC (660 HV) were used. A tungsten carbide ultrasonic carbide tip with a radius of 1.2 mm was pressed against the substrate with a static load of 4 kg and amplitude of 32 μm at a generator frequency of 20 kHz. During processing, the substrate was rotated at the speed of 3 m/min.

The cross-section of the SEM microstructure before and after ultrasonic nanocrystal surface modification (UNSM) processing is shown in Fig. 11. The modified area is marked with a dotted line in Fig. 11, *b* and 11, *e*. In this zone, the classical acicular microstructure of the martensite transforms into a fine-grained structure ~2 μm thick. In this case, the spherical particles of the carbides after processing do not undergo obvious changes either in size or in the distribution in the

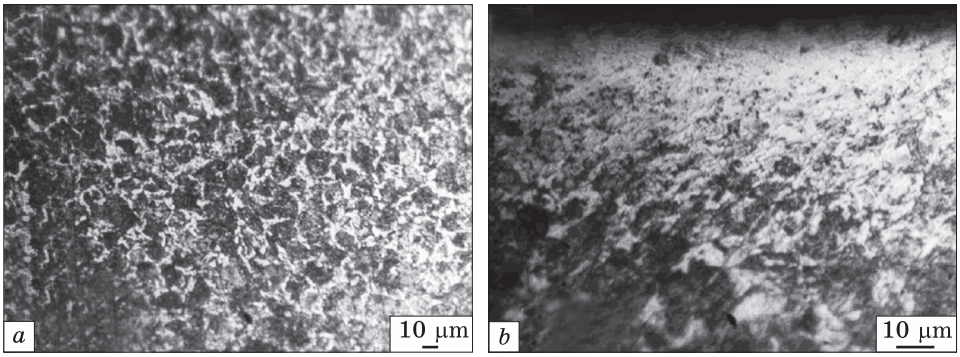

Fig. 12. Microstructures and features of S45C steel: *a* — before USP; *b* — after USP [17]

Fig. 13. Distribution of the microhardness: *1* — after US-treatment; *2* — before US-treatment [17]

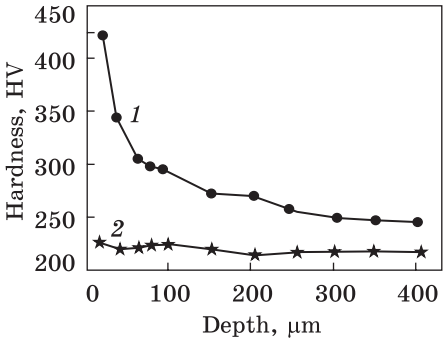

matrix. Introducing severe plastic deformation into the steel substrates used in this study enhanced the adhesion of the boron-doped diamond-like coating. This enhanced adhesion was attributed to the reduction in the hardness mismatch between the substrate and the coating as well as the gradient microstructural transformation layer.

In the work [17], a medium-carbon structural steel of average tensile strength (690 MPa), which is used for the manufacture of various parts, mechanisms, and structures in mechanical engineering and construction, has been investigated. The chemical composition of the steel (in wt.%): 0.45 C; 0.15–0.35 Si; 0.60–0.90 Mn; ≤0.030 P; ≤0.035 S; ≤0.30 Cu; ≤0.20 Ni; ≤0.20 Cr; and balance Fe. This steel has a b.c.c. structure with a high level of stacking fault energy (250 mJ/m^2). Ultrasonic processing (USP) was carried out in the rigid contact mode with the rotating polished cylindrical sample. The processing parameters were as follows: the frequency of the ultrasonic vibrations of the vibrator with a hemispherical tip made of WC (diameter 2.38 mm) was 20 kHz; the ultrasonic generator power was 1 W; the static load on the sample was 30 N; the impact amplitude was 30 microns; the number of the impacts N per mm^2 was 68000. The value of N was determined by the frequency f, the linear speed of rotation of the processed roller V (mm/s) and the speed of the ultrasonic striker movement S (mm/rev) according to the formula:

$$N = 60f/(VS). \quad (1)$$

Figures 12, *a* and *b* show the optical images of the pearlite-ferrite microstructure before and after deformation, respectively.

As can be seen from Fig. 12, *b*, the thickness of the deformed layer after severe US processing is 30–40 microns. The change in microhardness with depth is shown in the Fig. 13. The hardening effect is 188%.

In [18], the modification of the ferritic-martensitic steel EK-181 structure after ultrasonic finishing treatment (USFT) was investigated. The chemical composition of this steel (wt.%): 0.1–0.2 C; 0.3–0.5 Si; 0.5–0.8 Mn; 10–12 Cr; 0.1 Ni; 0.01 Mo; 1.0–2.0 W; 0.2–1.0 V; 0.2–1.0 V; 0.01 Nb; 0.05–0.2 Ta; 0.003–0.006 B; 0.02–0.15 N; 0.03–0.3 Ti; 0.01 Zr; 0.1 Cu; 9.01 Co, and balance Fe. Standard heat treatment of the rolled samples consisted of quenching from 1080 °C for 1 h and aging at 720 °C for 3 h. Ultrasonic treatment was carried out at the machining tool frequency of 24 kHz with an amplitude of 15 μm. The scanning step of the striker over the surface of the steel plate was ~0.3 mm.

After quenching and aging, EK-181 steel has a structure consisting of the fragmented packet martensite with a crystal transverse size of 270 nm (Fig. 14, *a*, *b*) and a grain/sub-grain structure of the α-phase (Fig. 14, *c*). A feature of this microstructure is the fact that the cellular-mesh dislocation substructure exists in the fragments of the martensite. The grain/sub-grain structure of the α-phase indicates the onset of the recrystallization during the hardened steel aging. In this case, Laves phases ($TiCr_2$ and Fe_2W) are precipitated, as well as special carbides $Cr_{23}C_6$ and V_2C. The total volume fraction of the secondary phases does not exceed 2%, with the main contribution being made by the Fe_2W phase. According to TEM studies, nanocrystalline particles of V_2C and $Cr_{23}C_6$ carbides are formed along the boundaries of the ferrite grains and fragments of the packet martensite, while particles of the Laves phase Fe_2W are located along the boundaries of the ferrite grains. Quantitative changes in the main structural parameters after various impacts are shown in Table 1. Substantial structural changes occur after complex processing, *i.e.*, quenching followed by ultrasonic processing and aging. In the surface layer, one can observe mainly the nanosize grain structure of the α-phase (Fig. 15) and the structure of the packet

Table 1. **Structural parameters of the steel after different treatments [18]**

Process	a, нм	ε	ρ, 10^{10} см$^{-2}$	R, нм	d, нм
Hardening + USFT	0.28755	0.0021	10	120	—
Hardening + aging	0.28724	0.0013	4.5	270	300
Hardening + USFT + aging	0.28733	0.0023	6.5	120	140

Note: a — is the crystal lattice parameter; $\varepsilon = \Delta d/d$ is the crystal lattice distortion; ρ — is the dislocation density; R is the average transverse size of martensite crystals; d — is the average size of dislocation-free ferrite grains.

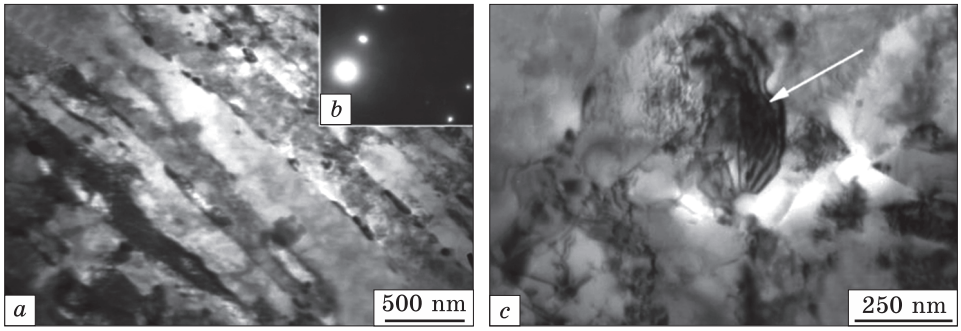

Fig. 14. The steel microstructure after standard heat treatment: *a* — fragmented packet martensite with particles of the special carbides along the boundaries of the fragments; *b* — microelectron diffraction pattern with reflections belonging to the (111) plane of the-phase reciprocal lattice; *c* — grain-subgrain structure of the α-phase. The arrow indicates the centre of recrystallization [18]

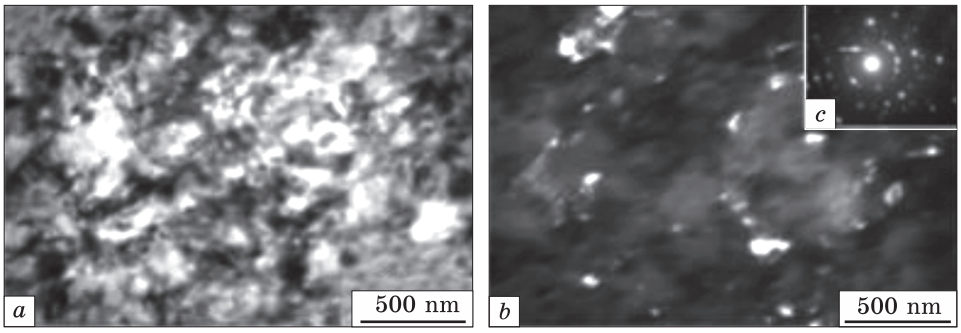

Fig. 15. Nanocrystalline structure of the α-phase in the surface layers of EK-181 steel subjected to quenching, US treatment, and aging: *a* — the bright-field image; *b* — the dark-field image obtained in the reflex [002]V_2C; *c* — microelectron diffraction pattern with an annular arrangement of the α-phase reflections; the arrow indicates the dark field reflex [18]

martensite. Compared with standard heat treatment, the transverse size of the martensite crystals decreases to 120 nm with a dislocation density of $6.5 \cdot 10^{10}$ cm^{-2}. In [19], the structure of the surface layer of the low carbon structural steel 20 after ultrasonic treatment was studied. The composition of the steel (wt.%): C 0.17–0.24; Si 0.17–0.37; Mn 0.35–0.65; Cu ≤0.25; Ni ≤0.25; As ≤0.08; S ≤0.4%; P ≤0.035; and balance Fe. This steel is used for the production of the lightly loaded parts (pins, axles, copiers, stops, gears), casehardened parts for the very long service life (operation at the temperature not exceeding 350°C), thin parts that work for abrasion. The structure of the annealed steel 20 consists of the mixture of structurally free polyhedral ferrite grains with a size of 5–15 microns (75% vol.) and pearlite colonies (Fig. 16). Pearlite grains of irregular size are evenly distributed over of the mi-

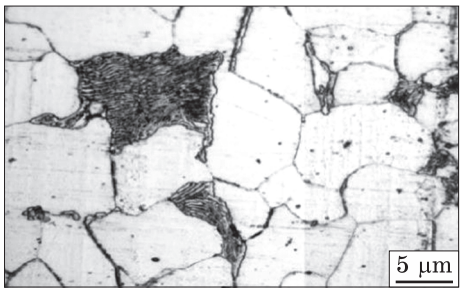

Fig. 16. Optical image of the original structure [19]

crosection surface. There are several pearlite colonies in large pearlite grains up to 29 microns in the size. Small grains with the pearlite structure, about 3 microns in size, mainly consist of the one pearlite colony with an imperfect structure. In addition to the ferrite and pearlite grains, individual grains of the tertiary cementite are observed in the steel structure in the form of the extended interlayers or globules located at the boundaries or the joints of the ferrite grains.

The samples were processed on the lathe with the ultrasonic set consisting of the ultrasonic generator and the magnetostrictive transducer with a waveguide having the soldered spherical striker (WC) with a radius 5 mm of the curvature. The tool was fixed in the lathe support. The processing was carried out at optimal modes: the generator power was 200 W, the striker oscillation amplitude was 10 μm, and the striker clamping force was 75 N. The peripheral rotation speed of the part was set to be equal to 125 rpm. The ultrasonic tool feed was 0.05 mm/rev.

A more detailed analysis of the modified microstructure was performed using TEM (Fig. 17). The structure includes two phases: the solid solution of carbon based on the b.c.c. iron lattice (ferrite) and the chemical compound Fe_3C with a complex orthorhombic crystal lattice (cementite). More subtle changes in the microstructure of intensely deformed steel 20 can be observed in TEM images (Fig. 17, 18). In Fig. 17, *a*, *d* shows the formation of the fragmented substructure in the grains of the structurally free ferrite with the high-angle misorientation of the sub-grains, as evidenced by the nature of the quasi-ring pattern of the microelectron diffraction patterns (Fig. 17, *b*, *c*). Two types of subgrains can be distinguished, characterized by different dislocation substructure. Dislocations are practically invisible in the sub-grains less than 0.1 μm in size. In the larger sub-grains (0.1–0.7 μm), the dislocation network substructure with a scalar dislocation density of $5.5 \cdot 10^{10}$ cm^{-2} is formed. In Fig. 17, *e*–*h* shows the ferrite grains with the fragmented substructure with an average fragment size of 0.5 μm. Changes in the cementite particles can also be noted. Nanosize particles of this carbide phase are located at the boundaries of the fragments, which are formed either because of the destruction of the carbide interlayers located at the boundary of the initial structure ferrite grains, or formed due to the cementite interlayers dissolution and secondary precipitation of the fine cementite particles. As a result of ultrasonic treat-

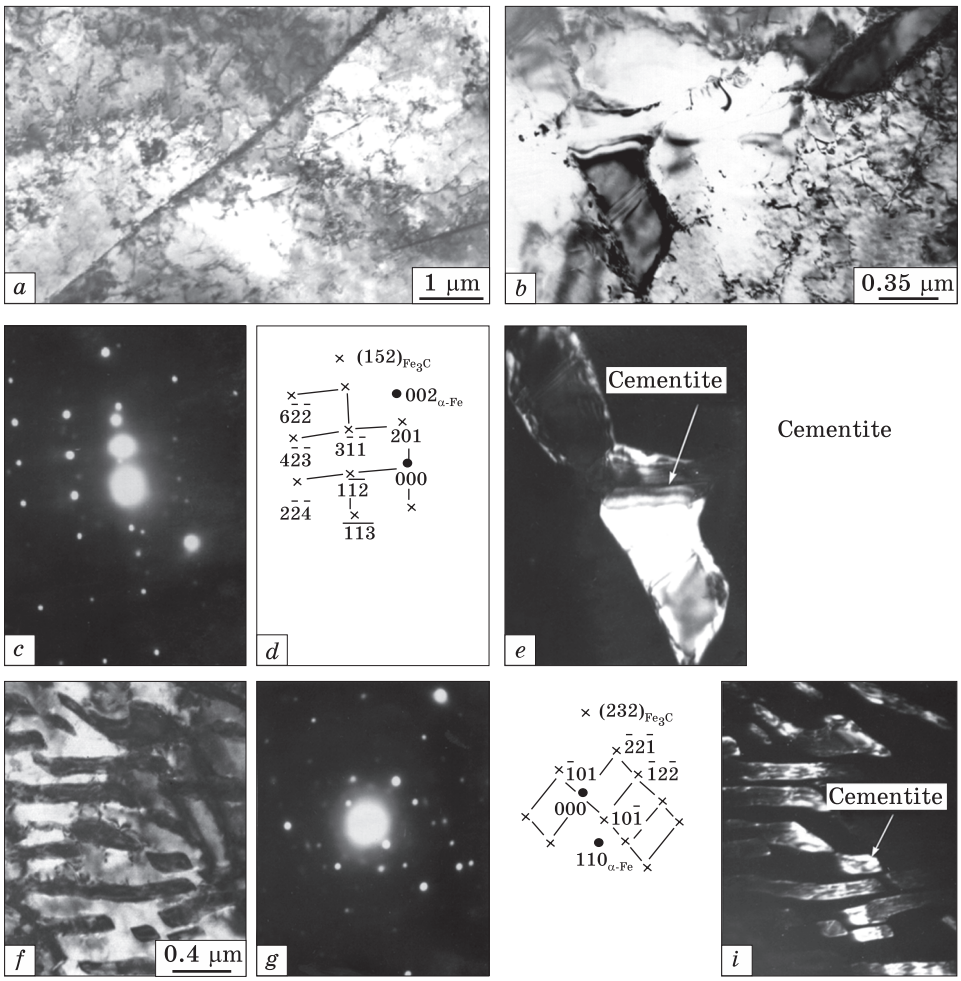

Fig. 17. TEM-image of the ferrite (*a*–*e*) and the pearlite (*f*–*i*) grains of steel 20: *a*, *b*, *f* — the bright field image; *c*, *g* — the microdiffraction pattern; *d*, *h* — the microdiffraction of the pattern diagram; *e* — the dark-field image in the reflection [201] Fe_3C microdiffraction *c*; *i* — the dark-field image in the reflection [221]Fe_3C microdiffraction *h* [19]

ment, large particles of the tertiary cementite located in the original structure at the boundaries of the ferrite grains (see Fig. 17, *b*, *e*) break into blocks of the submicron sizes (Fig. 17, *f*–*i*). In this case, the shape and size of the particles do not change. After severe deformation, transformation is also observed in the pearlite grains (Fig. 18). A fragmented substructure with a fragment size of ~0.3 μm is formed in the ferrite interlayers. There is also the cellular-mesh dislocation substructure with the scalar density of $4 \cdot 10^{10}$ cm^{-2} inside the fragments (Fig. 18, *c*) and the formation of the nanoscale cementite particles upon the des-

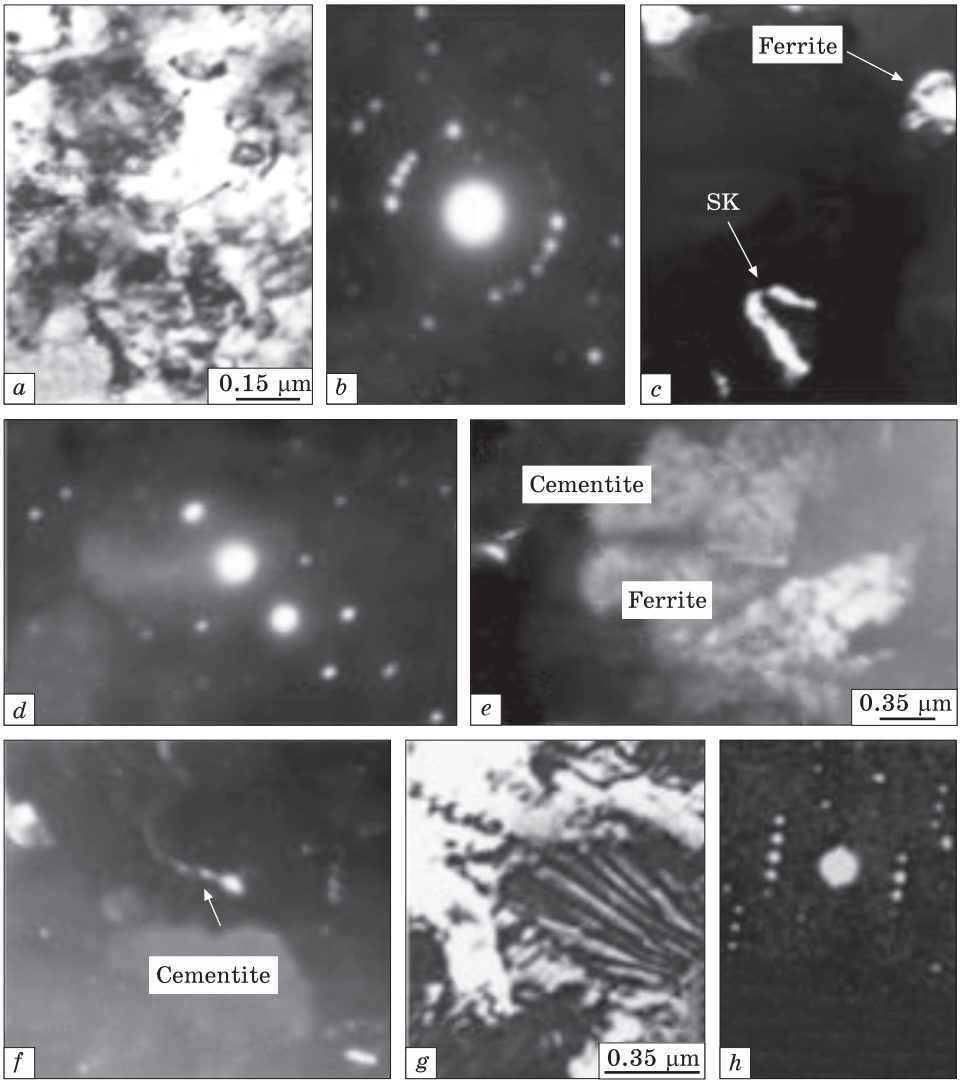

Fig. 18. TEM image of the ferrite grains on the steel 20 surface after US-treatment: *a*, *g* — bright-field image; *e* — dark-field image in reflex [011]αFe and [210]Fe_3C microdiffraction *d*; *h* — dark-field image in the reflex [112] Fe_3C microdiffraction *d* [19]

truction of the plates (Fig. 18, *e*). The microelectronogram obtained from such particles contains the reflections, the azimuthal blurring of which is ~ 10° (Fig. 18, *d*, *f*). The electron diffraction patterns also contain diffuse reflections belonging to the crystal lattice of the carbide phase (Fig. 18, *b*, *e*). An increase in the degree of the reflections blurring from the cementite phase after ultrasonic treatment can be noted (Fig. 18, *b, d, f*).

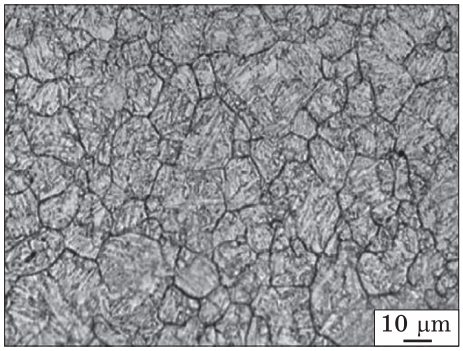

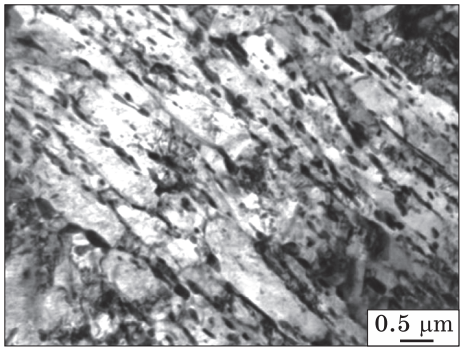

Fig. 19. Microstructure observation of S45C steel after quenching and tempering [20]

Fig. 20. Distribution of the carbides within the ferrite grains [20]

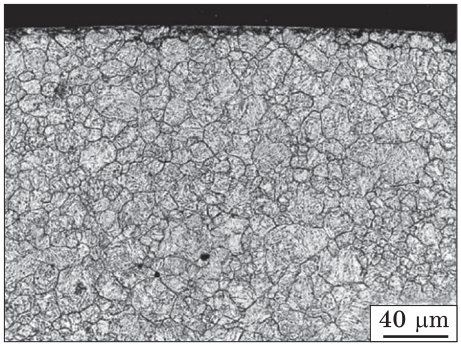

Fig. 21. The cross-sectional micrograph of the un-treated specimens [20]

In work [20], medium-carbon steel of the composition (wt.%): 0.45 C; 0.15–0.3 Si; 0.6–0.9 Mn; ≤0.03 P; ≤0.035 S; ≤0.3 Cu; ≤0.2 Ni; ≤0.2 Cr; and balance Fe. This steel is widely used in mechanical engineering, for example, for the manufacture of moving parts at high speeds. The microstructure of the sample after quenching and tempering is shown in Fig. 19 and is tempered sorbitol with an average grain size of about 20 μm. The TEM image (Fig. 20) shows the distribution of the carbides within the ferrite grains. Carbides are distributed in the direction of the acicular form of the martensite.

Ultrasonic processing of the rotating bar was carried out at the frequency of 20 kHz with amplitude of 30 μm. The tip of the striker/horn with a diameter of 2.4 mm, made of tungsten carbide, was pressed against the sample with the force of 50 N. Figures 21 and 22 show transverse SEM sections for two structural states of the samples. In these photos, after processing, a deformed zone with a thickness of 55 μm with subdivided grains is clearly visible. The x-ray in Fig. 13 with reflections (110), (210), (211) is typical for the b.c.c. ferrite. After processing, broadening of the reflections associated with the grain refinement and the appearance of the internal compressive stresses is seen. The corresponding hardening effects are shown in Fig. 23.

The authors [21] investigated high-strength low-alloy steel 300 M of the composition (wt.%): 0.38–0.42 C; Cr; 0.60–0.90 Mn; 0.30–0.50 Mo; 1.65–2.0 Ni; 1.45–1.80 Cu; 0–0.10 P; 0–0.10 S; and balance Fe. After

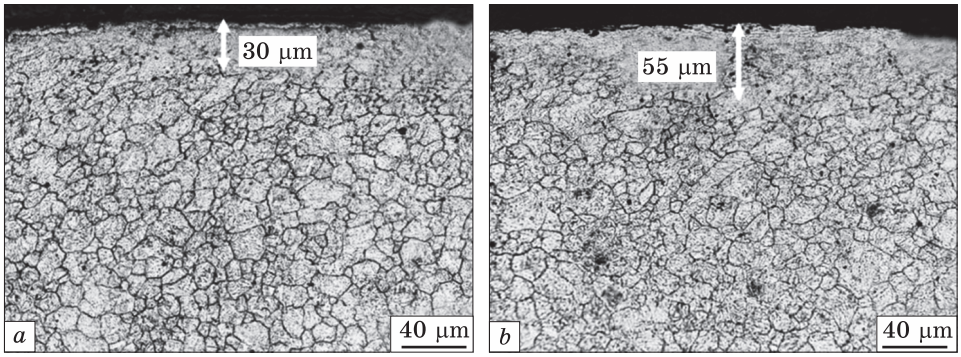

Fig. 22. The cross-sectional micrographs after US-treatment: *a*, U1 and *b*, U2 specimens [20]

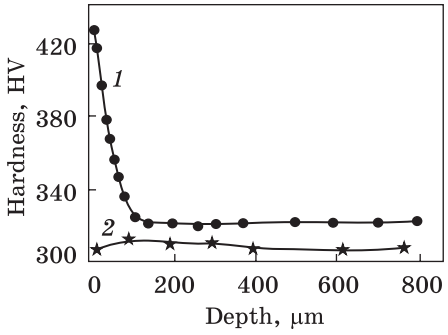

Fig. 23. The results of microhardness distribution along the cross-section of the specimens: *1* and *2* — after and before treatment, respectively [20]

quenching and tempering, it has a very good combination of strength and toughness, fatigue and ductility; used where fracture toughness and toughness are critical, such as high-performance auto parts, aircraft landing gear, airframe parts, high strength bolts, and any other high strength applications. To increase the wear resistance, additional finishing modification of the surface of the products is required. After standard heat treatment, the steel structure consists of the martensite with an average grain size of 2.3 μm.

For ultrasonic processing, the generator with a frequency of 20 kHz was used. The amplitude of the striker with the WC tip was 24 μm at the load of 30–50 N. In Fig. 24 shows x-ray diffraction patterns for the original (control) sample and after ultrasonic processing. As you can see, for the control sample (Fig. 24, *a*), three diffraction reflections α-Fe are observed: (110), (200), and (211). The presence of the same three diffraction peaks after deformation indicates the retention of the phase composition. However, as shown in Fig. 24, *b*, *c*, and *d*, compared to untreated samples, the diffraction peaks for treated samples become much broader. In addition, although there is no apparent change in the intensities of α(110) and α(211) before and after treatment, the intensity of the α(200) peak is significantly reduced. These results can be associated with grain refinement and the dislocation density increasing caused by SPD. Optical microscopy and SEM showed that the thickness

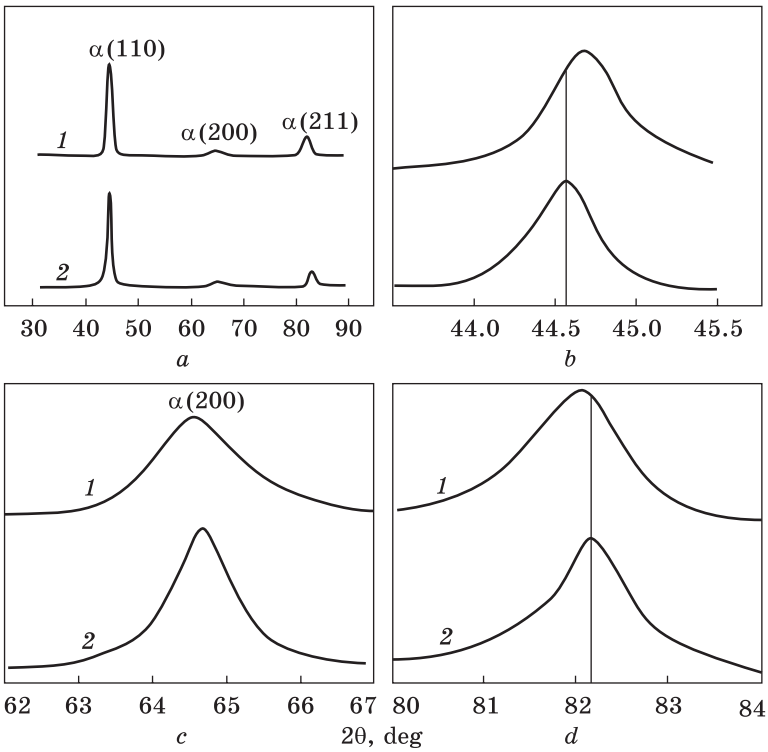

Fig. 24. (*a*) X-ray spectra for 300M steel: control (2) and US-processed sample (1) and amplified x-ray spectra for control and US-processed sample of (*b*) α(110), (*c*) α(200) and (*d*) α(211) [21]

of the deformed surface layer is 32 μm. In this layer, the martensite phase is refined. The grain size in the depth increases from 1.02 μm to 1.97 μm at the depth of 200 μm.

Figures 25, *a*, *b* show TEM images in the thinnest surface layer. A significant refinement of the martensite grains with an increased density of the dislocations after SPD is seen in comparison with the control sample (Fig. 26). The layer-by-layer distribution of the microhardness for two states of the structure is shown in Fig. 27. From the initial value of 567 HV, the microhardness increases to 797 HV after ultrasonic treatment. In addition, the wear resistance of the treated samples was significantly improved, which is associated with the grinding of the martensite plates, work hardening, and the residual compressive stress.

2.2. High-Frequency Impact Peening

The chemical composition of the 20GL grade low-carbon steel investigated in [22] was (wt.%): C 0.15–0.25; Mn 1.2–1.6; Si 0.2–0.4; S ≤ 0.04; P ≤ 0.04; and balance Fe. Prior to HFIP-treatment, samples

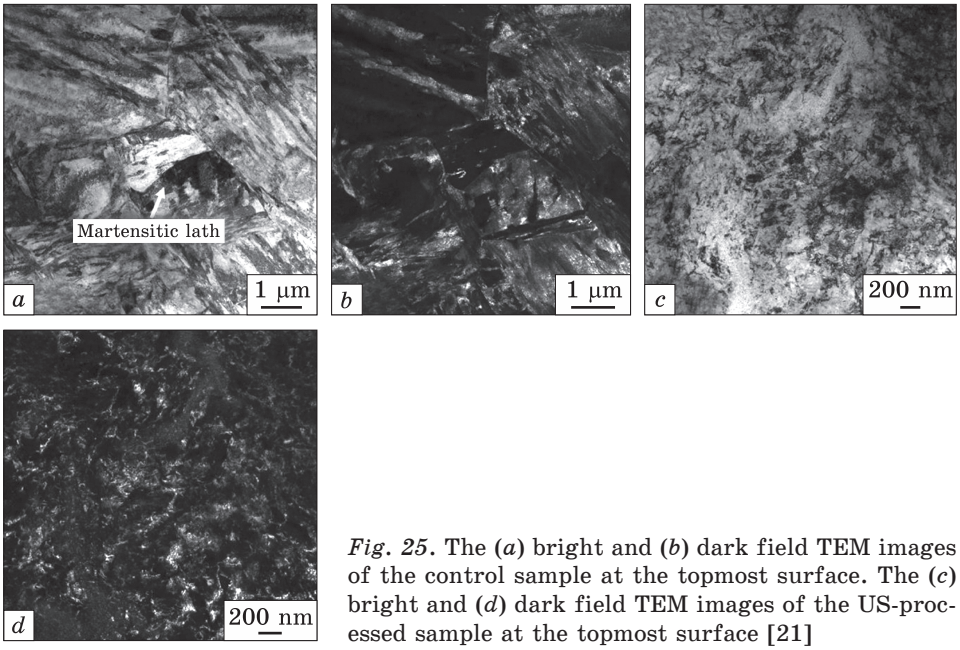

Fig. 25. The (*a*) bright and (*b*) dark field TEM images of the control sample at the topmost surface. The (*c*) bright and (*d*) dark field TEM images of the US-processed sample at the topmost surface [21]

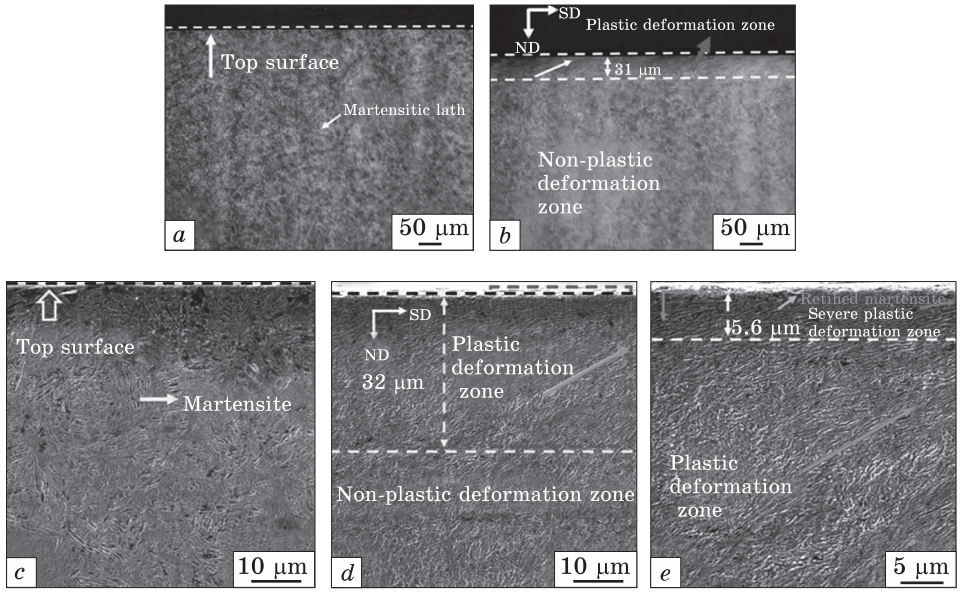

Fig. 26. Optical — images of cross-sectional microstructures for (*a*) control and (*b*) HF-processed 300M steels. SEM images showing cross-sectional microstructure of (*c*) control and (*d*) US-processed 300M steels. (*e*) Enlarged image of the area in (*d*) that is enclosed by dashed lines [21]

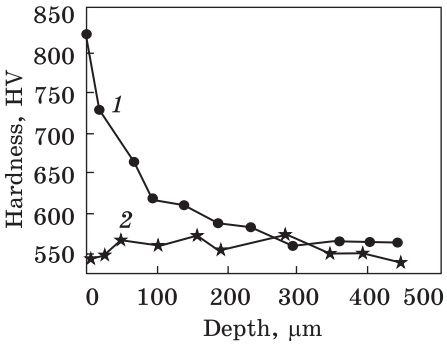

Fig. 27. Distribution of in-depth hardness in the initial (*2*) and US-processed (*1*) samples at 50 N and 250 mm/min [21]

of this steel were subjected to the normalized annealing. The processing was carried out under the following modes: generator frequency of 18.7 kHz; power of 4 kW; frequency of the striker made of hardened AISI 52100 steel of 3 kHz; amplitude of 33 μm; the speed of the striker movement on the sample surface was 3 m/s. The processing of the cylindrical samples was carried out on a lathe.

Results of metallographic analysis of microstructure in the pristine specimen denote the existence of the structural constituents usually observed in annealed low-carbon steels (Fig. 28, *a*). The microstructure consists of light ferrite grains and dark pearlite grains of similar sizes (~3...20 μm). The TEM images confirm that the grains with pearlite colonies contained mainly lamellar cementite and low scalar density of dislocations (of $5 \cdot 10^8$ cm^{-2}) (Fig. 28, *b*). The grains of ferrite, *i.e.*, a solid solution of carbon based on the bcc iron lattice, are also characterized by low dislocation density. Additionally, globular cementite precipitates of ~80–250 nm are frequently observed inside the ferrite grains and at the grain boundaries or junctions (Fig. 28, *c*).

TEM observations of the microstructure in the sub-surface layers of the HFIP-processed specimens show that the ferrite constituent undergoes substantial changes (Fig. 29, *a*) consisting in the formation of a dislocation-cell structure with the cell size of ~0.25–1 μm. Additionally, it shows that the strain extent in the surface layer studied is about 20–50%. According to the selective area electron diffraction (SAED) pattern, the azimuthal misorientation between the neighbouring cells is about 2–5° (Fig. 29, *b*). It is of importance that both the cell boundaries and the separate dislocations in the interior of the cells are blocked with fine precipitations (~20–40 nm) of a cementite type. High-angle boundaries between the ferrite grains, which were clearly detected in the pristine steel specimen (Fig. 28, *c*), become less pronounced in the subsurface layer after HFIP-treatment. Often, they appear as disclinations or boundary sections of various lengths. In some areas, they are gradually transformed into cell boundaries. At the same time, the pearlite constituent undergoes considerably less changes, which manifest themselves with the appearance of the dislocation tangles separating the ferrite lamellae. Additionally, the cementite lamellae also become interrupted in some areas, where they were cut by slipping dislocations (Fig. 28, *c*).

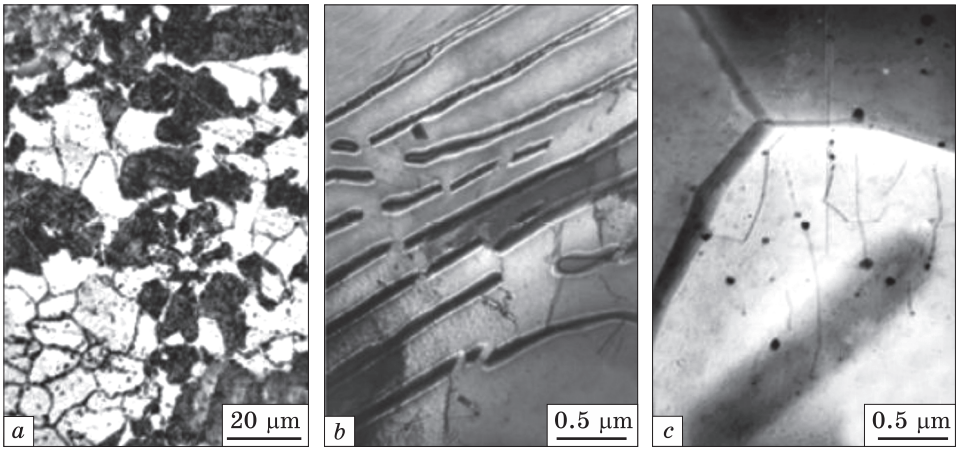

Fig. 28. The light microscopy image (*a*) and TEM — images of the pearlite microstructure (*b*) and the ferrite (*c*) phase constituents in the pristine specimen of 20GL steel in the initial state [22]

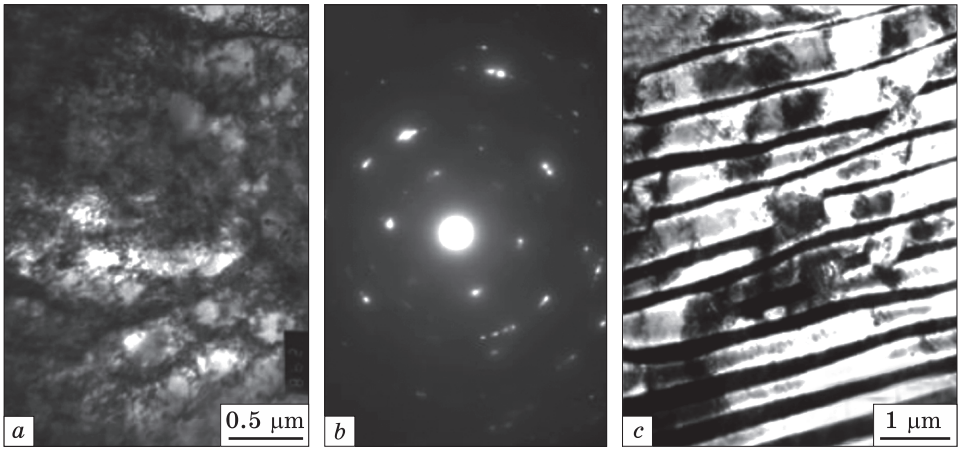

Fig. 29. TEM observations in the subsurface layer microstructure at a depth of 15–25 μm from the outmost surface after HFIP-treatment: the bright field image of the ferrite constituent (*a*), appropriate SAED pattern (*b*) obtained from (*a*), and the pearlite constituent (*c*) [22]

The dislocations are known to promote the dissolution of the carbon atoms into adjacent ferrite interlayers. Nevertheless, the fragmentation of the pearlite colonies is considerably smaller than that of ferrite grains. The SAED pattern also shows insignificant azimuthal diffusion (≤1.5°) of the diffraction spots obtained from ferrite lamellae in pearlite grains.

Structural changes caused by the HFIP-treatment led to a significant hardening of the surface layer, which can be seen from the nature of the layer-by-layer distribution of the microhardness (Fig. 30). The hardening effect is approximately 50%.

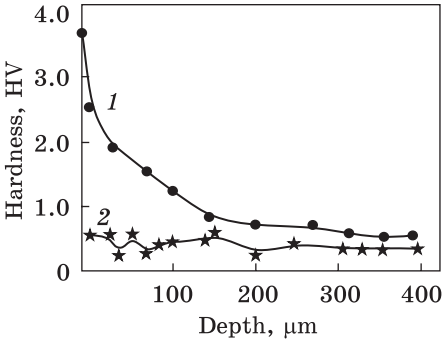

Fig. 30. Layer-by-layer distribution of the microhardness in the initial state (*2*) and after HFIP-treatment (*1*) [22]

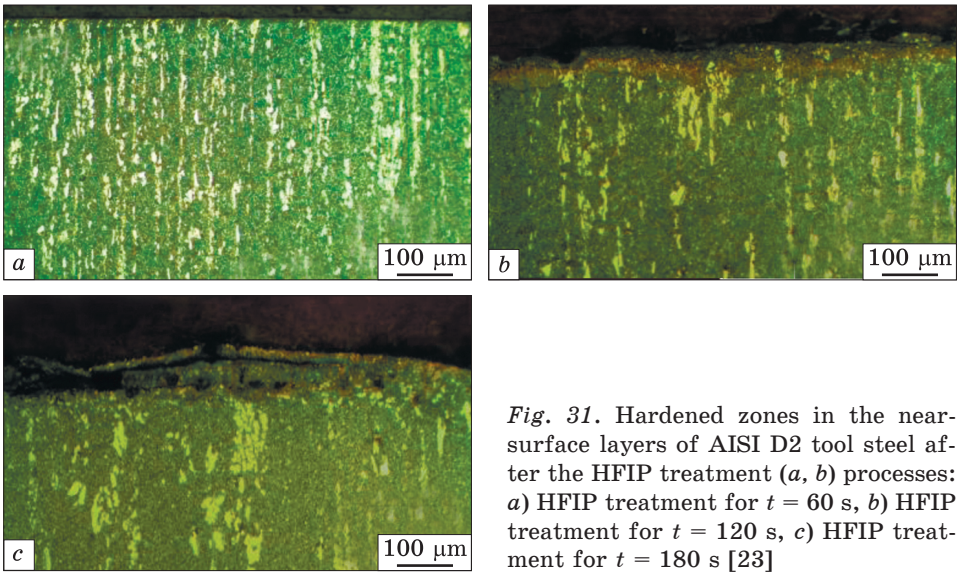

Fig. 31. Hardened zones in the near-surface layers of AISI D2 tool steel after the HFIP treatment (*a*, *b*) processes: *a*) HFIP treatment for t = 60 s, *b*) HFIP treatment for t = 120 s, *c*) HFIP treatment for t = 180 s [23]

In work [23], the high carbon tool steel AISI D2 of the following chemical composition (wt.%) was investigated: 11.5 Cr; 1.5 C; 0.83 Mo; 0.72 V; 0.46 Mn; 0.42 Si; 0.15 Ni; 0.06 Cu; and balance Fe. It is one of the most popular high chromium and high carbon D series steels, featuring high compressive strength and wear resistance, good quenching properties, high quenching stability, and good tempering resistance. This steel can be used as threading rolls and dies, ice trimming, cutting and punching tools for sheets up to 6 mm thick, tools for precision cutting of sheets up to 12 mm thick. Before treatment, the samples in the form of the plates were annealed at 850 °C, and then slowly cooled in an oven to 650 °C. The initial steel structure after heat treatment contained alloyed α-ferrite and carbide phases.

The HFIP treatment was carried out in the following modes: generator frequency 21.6 kHz; radiation power 53 mJ; the amplitude of the

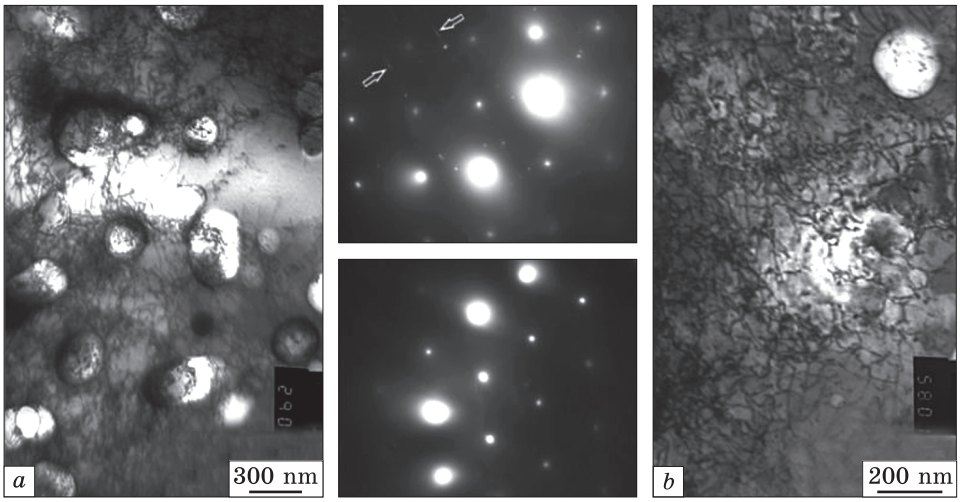

Fig. 32. TEM images of the microstructure and electron diffraction patterns of the tool steel AISI D2 in the initial state (*a*) and after HFIP process (*b*) [23]

striker with a diameter of 5 mm from hardened steel Fe–Cr15 15–18 μm at the frequency of 2 kHz; pressing force of the striker 50 N; processing time 60–180 s; striker movement speed 600 mm/min.

The length of the hardened layer (Fig. 31) depends on the treatment duration. At the depth of 18 μm, the microhardness as a result of processing increased by 1.5 times. This effect is explained by significant changes in the structural and phase states of the surface zone, confirmed by the data of x-ray diffraction and TEM analyses (Fig. 32). Comparison of x-ray diffraction spectra shows that changes in the phase composition occur in the surface layers of the studied steel at a depth of 10–20 μm. The x-ray spectra show lines of the trigonal chromium carbide Cr_7C_3 and/or complex carbide $(Cr, Fe)_7C_3$, as well as traces of the austenite and reflections of the α-phase. According to x-ray diffraction analysis, the total volume fraction of the carbides is about 5%, which is slightly less than the value (~10%) estimated using optical images of the microstructure in the cross-sections of the samples (Fig. 31). Analysis of TEM images (Fig. 32) showed the presence of the chromium alloyed ferrite with a dislocation density of $\sim 10^8$ cm^{-2}.

In addition, it contains a large number of light areas that are much thinner than that of the whole foil. Apparently, they formed in the places of etching and precipitation of the chromium carbides. These regions and the carbide particles remaining in the field of view indicate that the primary carbides were about 350 nm in size. The electron diffraction pattern in the selective region contains the system of the carbide reflections (indicated by white arrows). It should be noted that

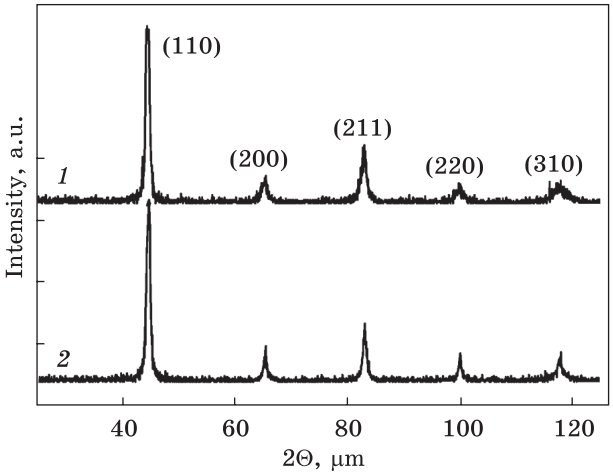

Fig. 33. Scheme of the x-ray patterns in the near-surface layer of AISI 1045 steel: after the HFIP process (*1*) and in the initial state (*2*) [24]

small spherical carbides are taken into account here. They are located in doped ferrite, in addition to large strip-like carbides, which were observed in optical images of cross-sections of the samples (Fig. 33).

Severe plastic deformation leads to a significant increase in the dislocation density (10^{10} cm^{-2}) and a slight decrease in the size and number of carbides in the microstructure of the surface layer 15–20 μm thick. The latter may be due to the deformation-induced dissolution of the carbon from carbide particles in the ferrite matrix. The dense dislocation networks are visible in sub-grains of the alloyed ferrite, the size of which is ~0.8 μm (Fig. 32, *b*). An increase in the number of defects in the crystal structure (density of dislocations, the number of vacancies, *etc*.), as well as fragmentation of the grains and carbides are manifested in an increase in the microhardness of the surface layer. After severe deformation, this increase is approximately 40–50% in comparison with the initial sample (Fig. 34).

Medium-carbon steel grade AISI 1045 (with composition (wt.%): C 0.45; 0.17Si; 0.52, Mn; 0.031; S; 0.032 P; and balance Fe) was investigated by the authors [24]. This steel is widely used in the industry due to its excellent combined properties, where higher wear resistance and strength are required. Typical applications include light gears, shafts, axles, spindles, pins, guide rods, connecting rods, bolts, worms, crankshafts, machine components, *etc*.

The steel plates were standardized with air-cooling. Before the HFIP treatment, the microstructure consisted of ferrite and pearlite. The ultrasonic generator with a frequency of 21.6 kHz and a power of $8.95 \cdot 10^{-3}$ J was used. The frequency of the striker with the diameter of 3 mm made of AISI 52100 steel was 2 kHz; exposure duration—60 s; amplitude — 18 μm.

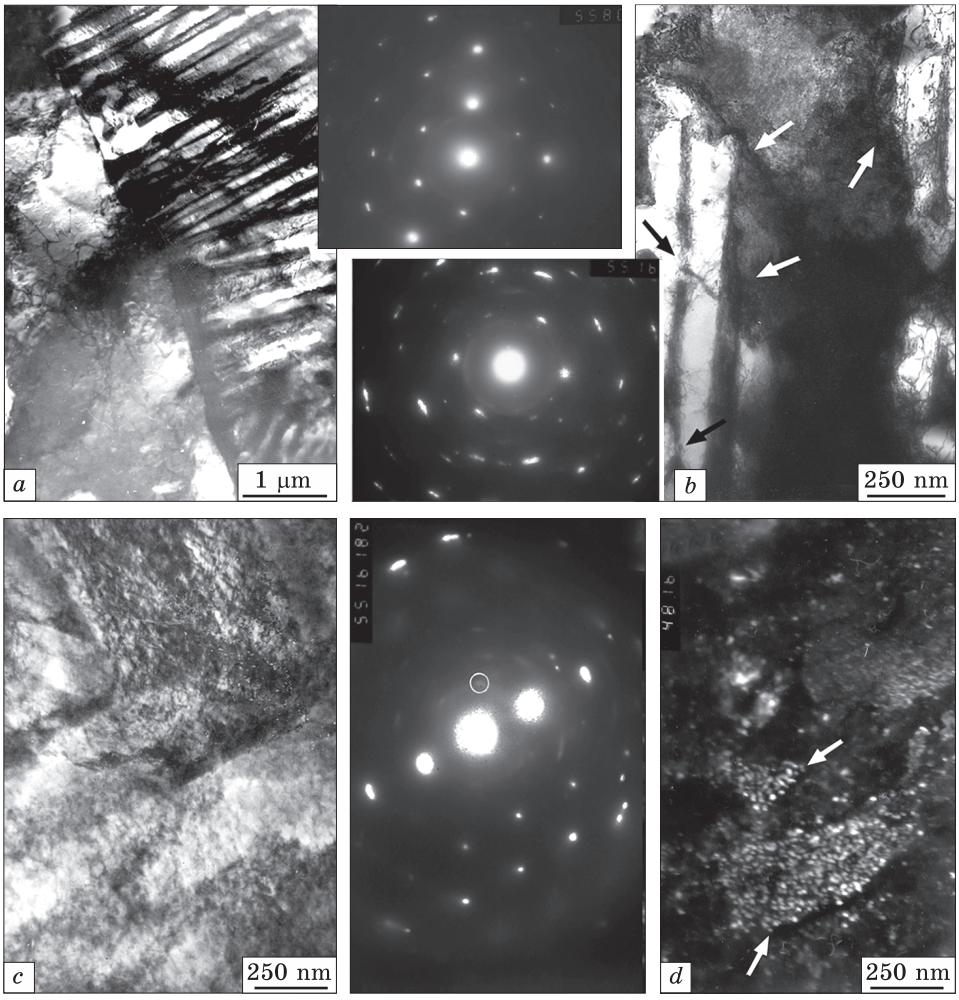

Fig. 34. TEM observations and appropriate SAED patterns of the microstructure in the top surface layers of 1045 steel specimens in the initial state (*a*) and after the HFIP treatment (*b*–*d*). The dissolution of the pearlitic plates (*b*) and the nanoscale cementite particles in bright-filed (*c*) and dark-field (*d*) images are indicated by arrows. The dark-field image was obtained from the cementite diffraction spot indicated by the circle [24]

Table 2. **Crystallite size D, lattice micro deformation η and dislocation density ρ in the initial state and after the HFIP treatment [23]**

Steel condition	*D*, нм	η	ρ_{XRD}, см/см^2	ρ_{TEM}, см/см^2
Initial	350	$1 \cdot 10^{-4}$	$4 \cdot 10^{8}$	$5 \cdot 10^{8}$
HFIP treatment	50	$2 \cdot 10^{-3}$	$5.6 \cdot 10^{10}$	$6 \cdot 10^{10}$

Fig. 33 shows the x-ray diffraction patterns for the initial state and after the HFIP treatment in the range of the diffraction angles 2θ = = 20–120°. As can be seen from this figure, this treatment does not make significant changes in the nature of the x-ray diffraction pattern in comparison with the original sample. As is known, SPD leads to the broadening of the diffraction peaks, due to both a significant decrease in the grain size and the appearance in the crystal lattice internal stresses. The latter can also be enhanced due to the oversaturation of the deformed grains/sub-grains of the iron matrix with carbon atoms diffusing from cementite particles and plates dissolved during deformation. The results of the analysis of such broadening effects for two states of the samples are given in Table 2. It is also important to note that the diffraction peaks in the x-ray diffraction patterns of the treated samples are shifted towards smaller diffraction angles, which indicates the formation of the residual compressive stress in the near-surface layer.

The TEM-microstructures characteristics in the uppermost surface layers (~10 μm) of the initial and samples after the HFIP treatment are shown in Fig. 34. The microstructure of the original sample consists of the ferrite grains and colonies of ferrite/pearlite plates mixture (Fig. 34, *a*). Ferrite grains ~1–5 μm in size and the ferrite interlamellar ferrite/pearlite colonies contain the dislocation networks and randomly located individual dislocations. Their density is low ($5 \cdot 10^8$ cm^{-3}) and correlates well with the assessment of x-ray diffraction analysis (Table 2). After SPD, a significantly deformed structure is observed in the surface layer. Intensive dissolution of the pearlite plates occurs in the ferrite/pearlite colonies. Along with this, carbon atoms and segregations (Cottrell atmospheres) follow dislocations moving in the ferrite components in azimuthally and radially dispersed the ferrite diffraction spots. Thus, the ferrite phase is saturated with carbon. Strongly dislocated ferrite grains (the density of dislocations is two orders of magnitude higher ($6 \cdot 10^{10}$ cm^{-3}) than that observed in the original grains. They already contain many subboundaries that subdivide their inner part into the submicron-scale blocks (Fig. 34, *c*). Moreover, the grain/subgrain boundaries are essentially decorated with newly formed nanosize cementite particles (see the dark-field TEM image in Fig. 34, *d*).

3. Processing with Accelerated Balls

3.1. Surface Mechanical Attrition Treatment

The authors [25] studied low-carbon steel of the following composition (wt.%): 0.11 C; 0.24 Si; 0.35 Mn; 0.018 P; 0.014 S; and balance Fe. The initial grain size of the annealed steel is in the range of 20...40 microns. Steel balls of 8 mm in size bombarded the surface of the samples with a frequency of ~ 3 kHz for 30, 60, 90, and 180 s. The grain size *D* after

processing was determined based on the analysis of the broadening of the x-ray b.c.c.-Fe reflections according to the Scherrer–Wilson formula [21]. The calculation results are shown in Table 3. As can be seen from these data, the average grain size decreases slightly with increasing processing time. Layer-by-layer x-ray analysis by layer-by-layer chemical etching showed that at the depth of 20 μm, the grain size is 46 nm. When the layer with the thickness of more than 40 microns is etched, the average grain size becomes $D > 1000$ nm. The layer-by-layer SEM image (Fig. 35) shows that the thickness of the deformed layer is about 50 μm for the processing time of 180 min.

According to the TEM analysis, the average grain size is 8 nm for the treatment lasted for 180 min, *i.e.*, it is lesser than that assessed according to x-ray analysis. This difference may be due to the fact that the XRD result averages information regarding the surface structure layer with a thickness of about 6 μm (for 95% absorption of CuK_α radiation), while TEM gives information from the layer of less than 1 μm thick (Fig. 36).

The silicon steel Fe–3.29Si ((Fe–3.29 Si–0.01 Mn, wt.%); high-strength steel (Fe–0.05 C–1.29 Mn) and eutectoid carbon steel Fe–0.80 C (Fe–0.80 C–0.20 Si–1.33 Mn) with the pearlite or the spheroidal structure were studied in [26]. The pearlite structure in Fe–0.80 C was obtained by austenitizing the samples at 1223 K for 30 min, and then holding at 873 K for 5 min to transform into pearlite. To obtain the spheroidite structure in Fe–0.80 C, the samples were austenitized at 1173 K for 60 min and quenched in the water to obtain the martensite.

The plane surfaces of the specimens were bombarded by shot peening with balls under the following conditions: steel shots (Fe–1.0 C–1.3 Si–1.0 Mn, wt.%) with a diameter of 50 μm and a hardness of 8 GPa were directed to the sample using an air compressor at the speed of 190 m/s at the distance of 10 mm. The process duration of 10–60 s provided the coverage of 1000–6000%.

Figure 37, *a* shows a SEM micrograph of the cross-section of the high-strength steel Fe–0.05 C–1.29 Mn after shot peening for 10 s. The initial structure is the fine-grained (~5 μm) ferrite. Two characteristic microstructural regions can be distinguished. One of them is the bright contrasting area near the surface, the structure of which is nanocrystalline according to the TEM results. The hardness of the near-surface surface is about 6.8 GPa. Another dark contrasting region with the

Table 3. **Average grain size *D* [25]**

Treatment duration, min	30	60	90	180
D, nm	33	28	23	27

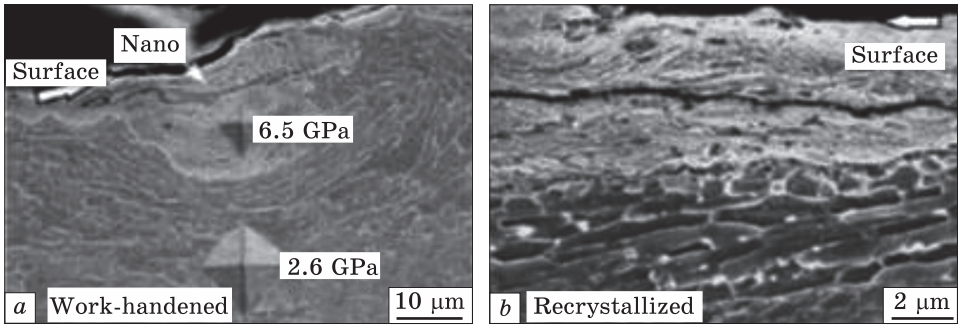

Fig. 35. Optical observation on the cross-section of the sample after the SP treatment for 180 min [25]

Fig. 36. TEM image of the top surface layer after the SP treatment for 180 min [25]

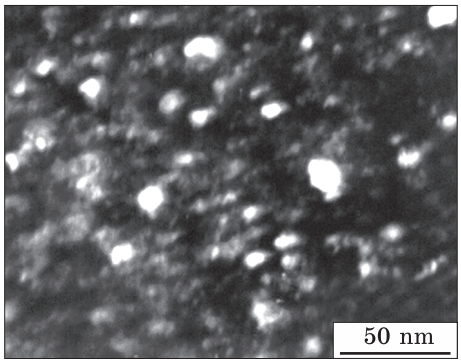

hardness of 2.6 GPa is in the strain hardening state, which is confirmed by the presence of the elongated grain boundaries. After annealing at 873 K for 60 min (Fig. 37, *b*), the nanocrystalline region did not show any noticeable changes, while the strain hardening regions immediately adjacent to the nanocrystalline region showed recrystallization. In the specimen subjected to processing with balls, the amount of the deformation is greatest in the upper surface zone and decreases with depth. The nanocrystallization can occur within a few microns from the upper surface, and below it, there is the strain hardening area. This so-called 'white-layer' is often observed in the severely deformed carbon steels [27–29] and cast iron [30].

Figure 38 shows the nanocrystalline surface layer formed in a Fe–0.80 C sample (pre-deformed by 84% by cold rolling) with the spheroidite structure after processing with balls. Before hardening with balls, spherical cementite particles with a diameter of about 0.5 mm were evenly distributed in the ferrite matrix. After processing, cementite particles are visible in the nanocrystalline surface layer. Figure 38, *b* shows the micrograph obtained using SEM after annealing at 873 K. It can be seen that no changes are noticeable in the nanocrystalline surface layer, while the subsurface layer in the strain-hardened zone shows the presence of recrystallization. In this case, the sample was preliminarily deformed and, therefore, recrystallization covers the entire volume of the sample, except the nanocrystalline region.

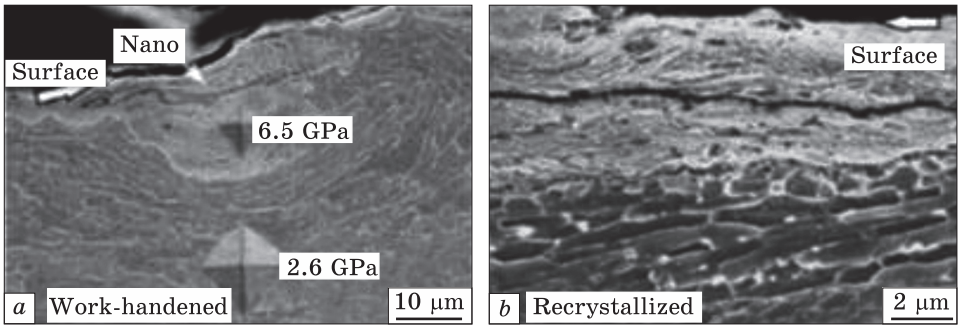

Fig. 37. SEM micrographs of Fe–0.05C–1.29Mn high tensile strength steel after SP for 10 s. *a* — after SP, and *b* — annealed at 873K for 3.6 ks after SP [26]

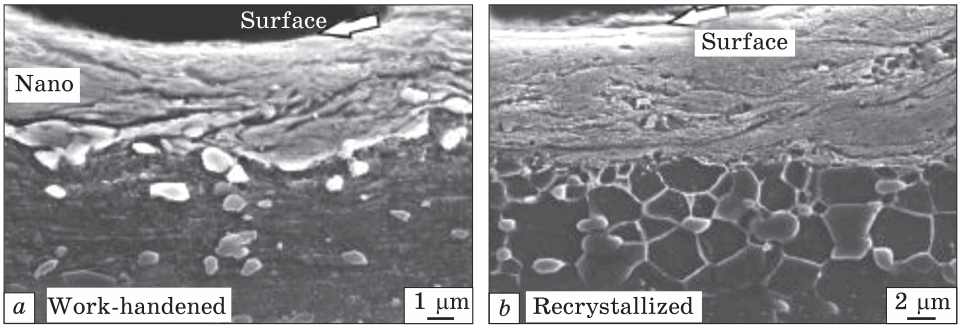

Fig. 38. SEM micrographs of of the nanocrystalline regions formed in prestrained (82% cold rolling) Fe–0.80C specimen with spheroidite structure by shot-peened for 10 s. (*a*) As shot-peened and (*b*) annealed at 873 K for 3.6 ks after shot peening [26]

For processing by the SMAT method in [31], samples were prepared from high-carbon ball-bearing steel AISI52100 with the composition (wt.%): 1.0 C; 1.5 Cr; 0.31 Mn; 0.24 Si; 0.08 Ni; 0.15 W; 0.03 Mo; and balance Fe. After spheroidization annealing, the structure of this steel contains the spheroidal cementite particles ranging in the size from 1 μm to 200 nm, embedded in the ferrite matrix with a grain size of about 15 μm. The volume fraction of uniformly distributed cementite particles is about 16%.

The SMAT process was carried out for 60 min in the vacuum chamber vibrated at a frequency of 50 Hz. Steel balls with a diameter of 8 mm are made of AISI52100 steel. The TEM structure after processing (Fig. 39) shows the uniform distribution of the nanostructure of the ferrite phase with the average grain size of 8 nm. Electronic microdiffraction does not record the presence of the cementite particles due to their small size or complete destruction during the process of severe deformation.

In [32], the steel sample was treated in vacuum ($6 \cdot 10^{-2}$ Pa) at ambient temperature for 60 min with the oscillation frequency of 50 Hz

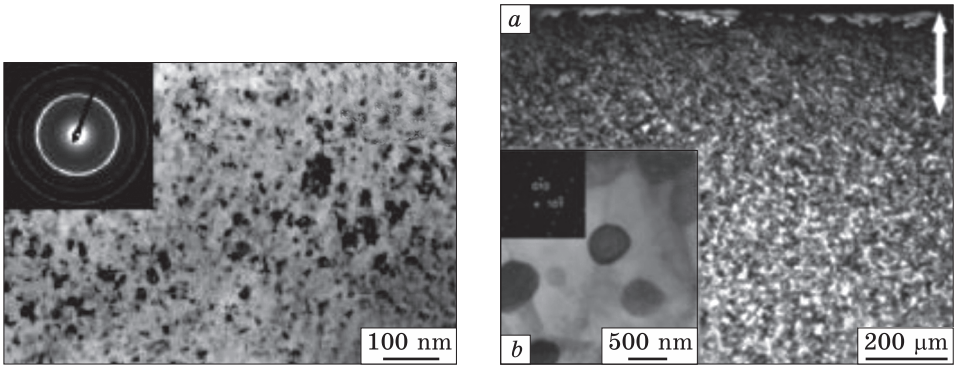

Fig. 39. Bright-field TEM- images for the as-SMAT sample. The corresponding selected electron diffraction patterns are shown in inset [31]

Fig. 40. *a* — the cross-sectional optical metallograph of the spheroidized steel after SMAT for 60 min; *b* — bright-field TEM-image of the as-annealed steel showing spheroidal cementite particles uniformly embedded in ferrite matrix. Inset in *b* is an electron diffraction pattern from a cementite particle [32]

(SMAT method). Steel balls 8 mm in diameter with the same chemical composition as the treated steel plate were used to eliminate contamination of the treated sample. The chemical composition of the investigated steel was (wt.%): 1.0 C; 1.5 Cr; 0.31 Mn; 0.24 Si; 0.08Ni; 0.15 W; 0.03 Mo; and balance Fe. The microstructure after annealing consists of the spheroidal cementite particles ranging in size from 1 μm to 200 nm, embedded in the ferrite, the average grain size of which is 15 μm (Fig. 40, *b*). The particles of cementite are evenly distributed in the ferrite matrix, and the distance between cementite is in the range from several hundred nanometers to several millimetres with a total volume fraction of 16%. In the annealed state, the cementite particles are dislocation-free single crystals, which are confirmed by transmission electron microscopy (TEM). The SEM cross-section (Fig. 40, *a*) shows signs of the plastic deformation in the near-surface layer of 250 μm thick, the microstructure of which differs from the microstructure of the matrix volume. TEM observations allow the assessment of more subtle structural changes in different the zones of the treated surface layer.

In the deeper layers of the deformed layer (150...250 microns), changes affect only the soft ferrite phase, while the cementite particles remain unstrained. The deformation of the ferrite is associated with the high activity of the dislocations, which originate at the interface between the ferrite and the cementite. It is here that the highest stress level arises, due to the large difference in the strength of the ferrite and the cementite in comparison with the interfaces between ferrite grains. As a result, there are driving forces for the generation of the dislocations and the dense dislocation walls (DDW) in the ferrite phase. In the

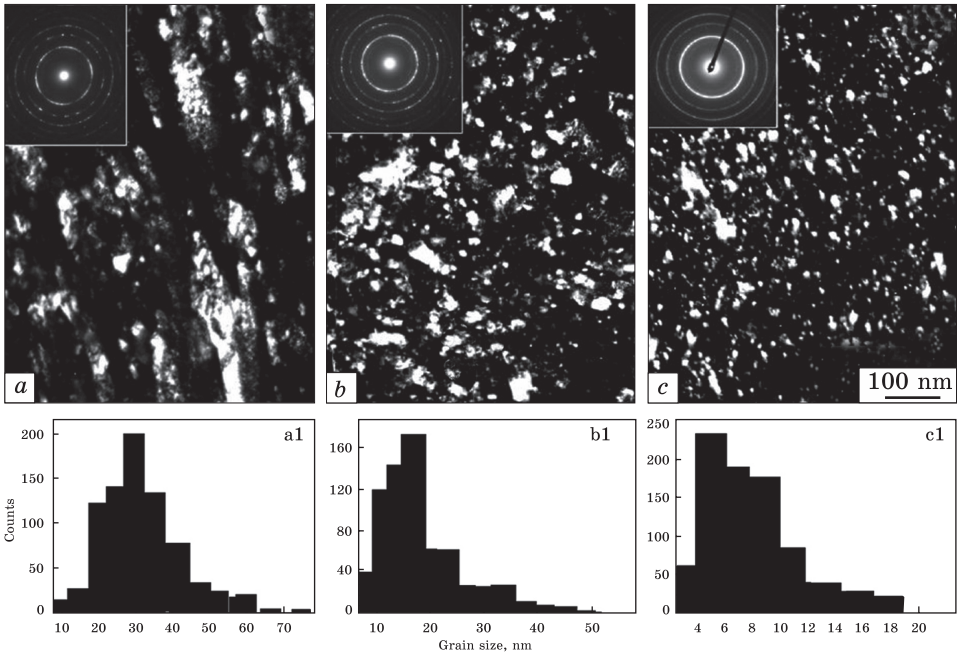

Fig. 41. Typical cross-sectional TEM dark-field images and corresponding SAED patterns (inset) together with the statistical grain size distributions (determined from TEM images) at different depths: (*a*, *a*1) ~35 μm; (*b*, *b*1) ~15–20 μm; (*c*, *c*1) ~5 μm [32]

upper deformed layers (160 μm), where the deformation extent is higher, more DDW and the dislocation cells are formed. As a result, they are gradually transformed into sub-grain boundaries (with small angles of misorientation) or the grain boundaries in the ferrite matrix. At this depth, the cementite particles also remain undeformed. The presence of many dispersed cementite particles, which greatly facilitate the nucleation of the dislocations in the ferrite during deformation, contributes to the refinement of the ferrite grains.

When the local stress concentration exceeds the critical shear strength of the cementite (depth <150 μm), dislocation slip systems are activated inside the cementite particles. It is interesting to note that the onset of plastic deformation of the cementite occurs in those areas in areas where ferrite grains are reduced to a size smaller than the cementite particles. Deformation and grinding of cementite particles were found in the surface layer with a depth of <150 microns.

Figure 41 shows typical cross-sections of TEM images in the dark field and corresponding SAED patterns in the nanostructured layer at different depths. It can be seen that the grain size gradually decreases with decreasing depth. In the upper layer with a depth of <5 μm, the grain size is <20 nm with an average value of 8 nm. According to TEM

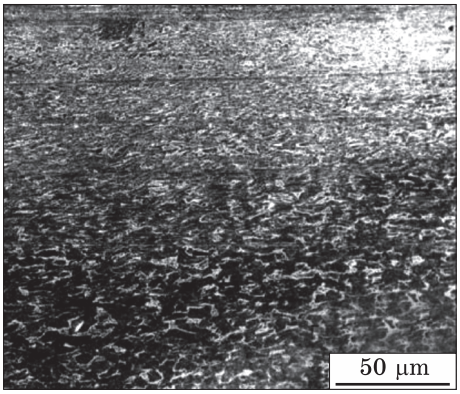

Fig. 42. The cross-sectional SEM observation of the SMATed sample [35]

analysis, the volume fraction of the cementite significantly decreases with increasing deformation (*i.e.*, with decreasing depth) from 16% for the bulk of the alloy to 7% at the depth of 60 μm. Closer to the upper surface layer (at the depth of <40 μm), electron microdiffraction does not detect the presence of cementite particles). The effect of the cementite dissolution was established earlier during the usual plastic deformation of pearlitic steels [33, 34]. Gridnev and Gavriljuk [33, 34] suggested that the dissolution of the cementite is caused by the sliding of dislocations in the cementite. This is due to the fact that the binding energy between the C and Fe atoms in the cementite is lower than the interaction energy between the C atom and the dislocation. Consequently, moving dislocations can capture C atoms with the decrease in the cementite size during plastic deformation and their transformation into ferrite.

The authors [35] investigated structural low-carbon steel of the ss400 grade of the following chemical composition (wt.%): C 0.171; Si 0.09; Mn 0.36; Al 0.025; Cu 0.01; Cr 0.02; Mo 0.01; Ni 0.03; P 0.013; S 0.013; and balance Fe. This steel is used for the manufacture of structural pipes, rods and other profiles.

The surface mechanical attrition treatment (SMAT) was used to modify the steel surface. Steel balls with a diameter of 8 mm positioned in the stainless-steel chamber vibrating at a frequency of 50 Hz, producing multiple impacts on the sample surface. In this case, the rate of the severe deformation of the surface layer lasting 15 min reaches the value of 10^3 s^{-1}. Figure 42 shows the SEM image of the cross-section of the processed sample. The depth of the deformed layer is about 80 μm. There are no pores or cracks in it. Typical TEM structures in the layer positioned at a depth of 1 μm are shown in Fig. 43. Obviously, the microstructure is characterized by nanoscale equiaxed grains with random crystallographic orientation, as indicated by the selected area electron diffraction diagram pattern (SAED). The histogram shows the narrow grain size distribution, as shown in Fig. 43, *c*. In accordance with the dark-field image, the average value of the grains in the specified layer is ~12.7 nm, which confirms the formation of the nanoscale structure during severe plastic deformation. During SMAT, deformation induced grain refining consists of the ferrite and the cementite grinding

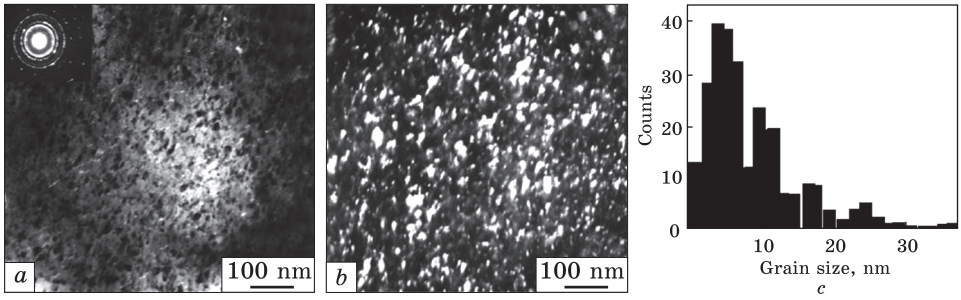

Fig. 43. a — bright-field and *b* — dark-field TEM images; *c* — static distribution of the grain size derived from the dark-field TEM-images showing plane-view microstructure of the top layer in the SMATed sample (insert is the corresponding SAED pattern) [35]

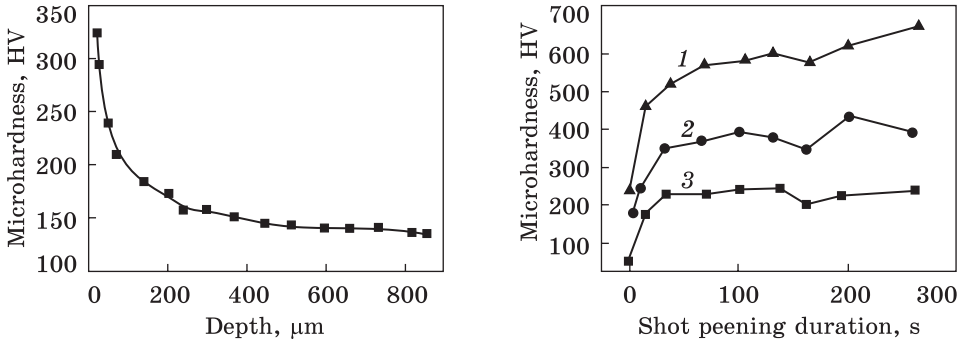

Fig. 44. Distribution of the microhardness with the depth from the treated surface after SMAT [35]

Fig. 45. Surface hardness profiles of the three carbon steels as a function of the SP treatment time: 1 — 0.8% C; 2 — 0.45% C; 3 — 0.1% C [37]

for ss400 carbon steel with the cementite particles and/or plates dispersed in the ferrite matrix. For ferrite in the given sample, the grain refinement includes the formation of the dense dislocation walls and dislocation clusters in the initial coarse grains, as well as in the subdivided crystallites/cells (with further deformation), the transformation of these microstructures into sub-boundaries with low-angle misorientation and the evolution of the sub-boundaries into highly misoriented grain boundaries.

The ferrite grinding process is greatly facilitated by the presence of dispersed cementite particles and/or plates since the cementite/ferrite interfaces are effective centres of the dislocation nucleation, as well as the barriers to dislocation movements. With the progressive nanostructuring of the ferrite phase with increasing deformation, the ferrite matrix is substantially work hardened. Multiple sliding gradually transforms the cementite into the nanosize cementite particles and/or plates

mixed with ferrite nanograins in the upper surface layer [36]. The significant hardening effect of the surface layer demonstrates the nature of the layer-by-layer distribution of microhardness in Fig. 45. As you can see, the microhardness increases by 2.5 times.

3.2. Air Blast Shot Peening

The authors of [37] studied three types of steel: low-carbon AISI 1010, medium-carbon AISI 1045, and high-carbon eutectoid steel. Chemical composition of AISI 1010 steel was (wt.%): 0.08–0.13 C; 0.30–0.60 Mn; ≤0.040–0.13 P; ≤0.050 S; and balance Fe. It mainly used for the production of cold-formed fasteners and bolts. The AISI 1045 steel ((wt.%): 0.312 C; 0.189 Si; 0.852 Mn; 0.025 Cr; 0.033 Mo; 0.005 Ti; 0.004 V; 0.033 W; 0.039 P; 0.011 S; 0.031 Cu; 0.037 Al; and balance Fe) is widely used for all industrial parts requiring greater wear resistance and strength. Typical applications for AISI 1045 are gears, pins, frames, shafts, rollers, axles, spindles, *etc*.

Before shot peening, the samples underwent normalizing annealing. For processing, RCW balls with a diameter of 250 μm and the hardness of 760 HV were used. The air pressure of 0.8 MPa provided Almen with an intensity of 0.06 mmA.

Fig. 45 shows the microhardness dependence on the processing duration for three grades of steels. This figure shows that the microhardness increases with increasing carbon concentration and reaches saturation in about 30–60 s. The maximum surface hardness for steels of 0.45% C and 0.8% C is observed after 60 s of treatment and is about 440 HV and 640 HV, respectively.

Figure 46 illustrates optical micrographs of the steel surface cross-section before and after deformation processing for 60 s. Before shot peening, the ferrite takes up most of the structure, while the pearlite fraction occupies the rest of the structure. As the carbon content increases, the portion of the pearlite increases, and the portion of the ferrite conversely decreases. Due to severe plastic deformation, the grains in the surface layer about 15 μm thick are severely deformed. In the case of 0.8% C steel, the only pearlite phase is observed prior to shot peening. However, after processing, the grains on the surface are transformed into a lamellar structure.

Figure 47 shows the x-ray diffraction pattern of steels depending on the treatment duration (30, 90, 150, and 240 s). The exposure time in Fig. 47 corresponds to those shown in Fig. 47. It is noticeable that the Bragg peaks become broader with increasing exposure time. The observed reflection broadening is associated with grain refinement and the accumulation of plastic deformation inside the grains. More subtle structural changes are visible in TEM images obtained from the depth

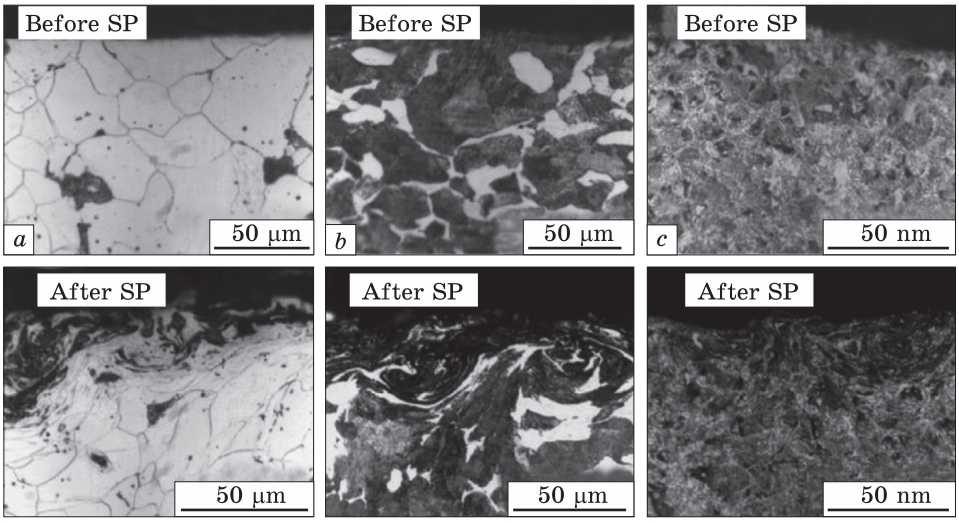

Fig. 46. Cross-sectional optical micrographs showing the microstructural evolu tion before and after shot peening for 60 s: (*a*) 0.1% C (*b*) 0.45% C, and (*c*) 0.8% C steels [37]

of 1 μm (Fig. 48). Distributions of the high-density dislocations caused by severe local plastic deformation are seen. Analysis of TEM images showed that after processing the average grain size is 350 nm for steel with 0.1% C, 234 nm for steel with 0.45% C and 130 nm for steel with 0.8% C. These data indicate that the grain refinement progresses as the carbon content increases.

The cross-sectional TEM images in Fig. 49 show the grain refining and cementite dissolution at three different depths from the top surface of 0.45% carbon steel. Figure 49, *a* shows that at the depth of 12 μm from the outmost surface the average grain size of the ferrite is 350 nm. The cementite size is estimated to be ~500 nm. This is due to the fact that intense hardening transforms the lamellar cementite in pearlite into spheroidal shape with partial dissolution in the ferrite. At the depth of 6 μm from the upper surface (Fig. 49, *b*), the average ferrite grain size is 330 nm, which is relatively large, taking into account the difference in depths in Fig. 49, *a* and *b*.

However, the size of the cementite is reduced to 160 nm while maintaining a small amount of the cementite. Meanwhile, Fig. 49, *c* shows that the ferrite grain size on the upper surface is about 230 nm, and most of the cementite disappears. Thus, it can be concluded that the deformation extent is sufficient for the cementite dissolution. Thus, it can be concluded that the surface hardening of the carbon steel during SPD increases both due to grain refinement and because of the dissolution of the carbon after cementite spheroidization.

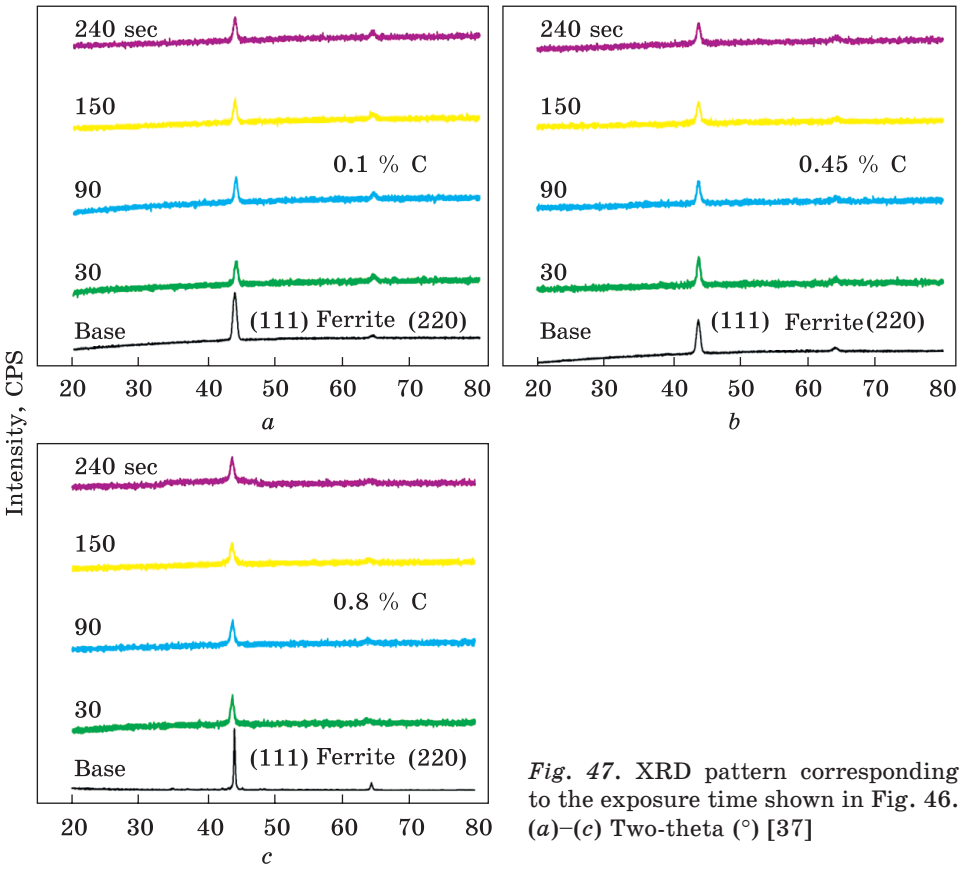

Fig. 47. XRD pattern corresponding to the exposure time shown in Fig. 46. (*a*)–(*c*) Two-theta (°) [37]

The authors [38] investigated the medium-carbon steel AISI 1050 with the chemical composition (wt.%): 0.51 C; 0.64 Mn; 0.23 Si; 0.16 Cr; 0.14 Cu; 0.02 Mo; Ni 0.07; S 0.005; Al 0.01; and balance Fe. This grade of steel is used for blades, brackets, brake discs, clamps, clutches, springs, washers and gears, and for the wide variety of mechanical engineering applications where the good combination of strength, toughness and wear resistance is required.

The samples were austenitized at 850 °C for 1 h, quenched in oil, and then held at 520 °C for 1 h, followed by cooling in air. The average hardness of the resulting microstructure is 28 HRC (285 HV). Figure 50, *a* shows the microstructure of AISI 1050 before heat treatment (in the state after annealing), while the pearlite phases (dark phase) and the ferrite (light phase) are clearly visible. After heat treatment (Fig. 50, *b*) (quenching and tempering), the boundaries of the pearlite and ferrite disappear, the portion of the ferrite decreases, and the portion of pearlite structure increases.

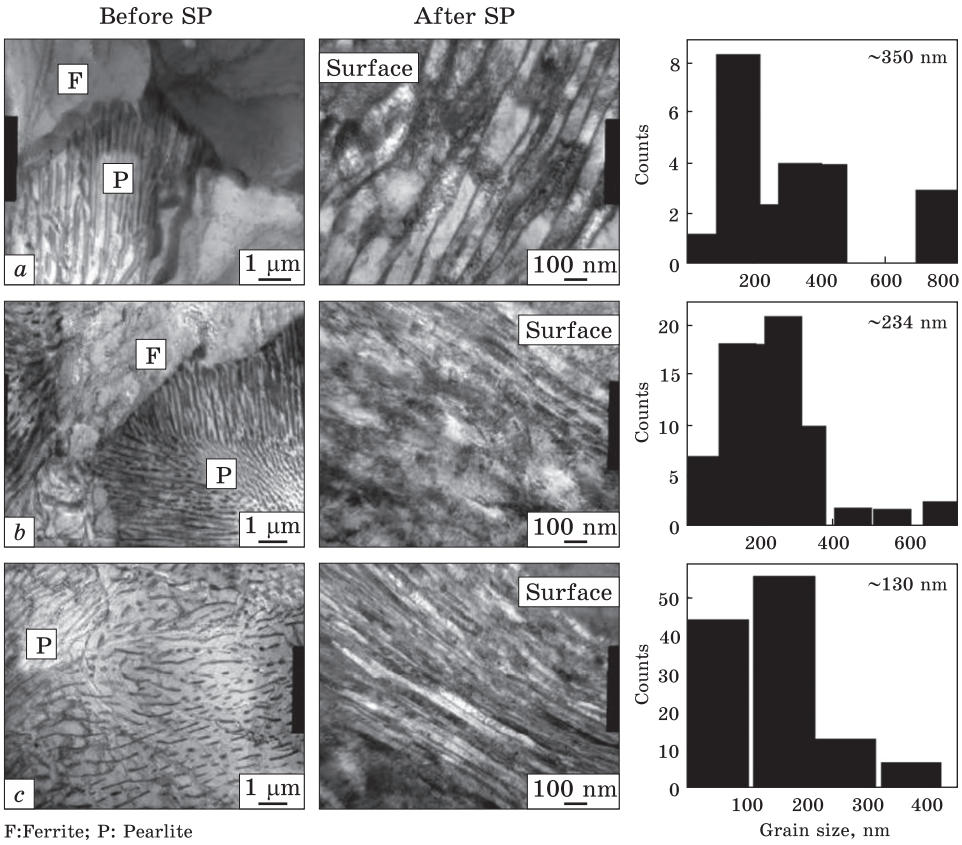

Fig. 48. Cross-sectional TEM — images covering the distance from the top surface to 1 μm below the surface and the grain size distribution along the distance (1 μm). The exposure time was 60 s for (*a*) 0.1% C, (*b*) 0.45% C, and (*c*) 0.8% C steels [37]

Shot peening was carried out with steel balls (hardness of 50 HRC) at the angle of 90° at the air pressure of 5.5 bars with a coating of 1500% and Almen intensity of 0.26. Structural modification after processing is shown in Fig. 51 and Fig. 52 (OM and SEM, respectively). These images demonstrate the formation of the ultrafine and nanostructured layers as a result of deformation. The minimum grain size is 50 nm according to the analysis of x-ray reflections using the well-known Scherrer's equation (Fig. 53). The layer-by-layer distribution of the microhardness after surface treatment is shown in Fig. 54. The maximum hardening effect is about 200%. At the depth of 700 microns, the bulk value of the microhardness is achieved.

Study of the low-carbon structural steel AISI 1020 of the following composition (wt.%): C 0.30–0.60; Mn 0.18–0.23; S 0.05; P 0.04; and balance Fe, is described in work [39]. AISI 1020 steel is used in a vari-

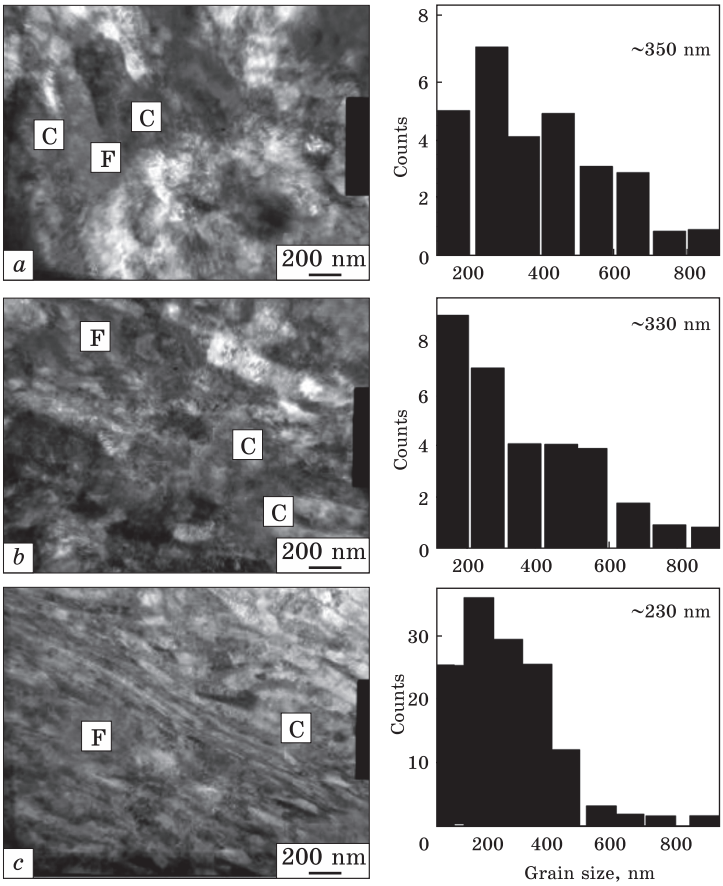

Fig. 49. Cross-sectional TEM - images that show the grain size refinement and the cementite dissolution at different depths for the 0.45% C carbon steel (*a*) at 12 μm deep from the surface, (*b*) at 6 μm deep from the surface, (*c*) at the surface, and [37]

ety of applications due to its good ability for cold drawing or turning and polishing properties. It is used for simple structures such as cold head bolts, shafts, lightly loaded gears, wear resistant surfaces.

The AISI 1020 steel samples were treated by mechanical attrition (SMAT) for 90 min, varying the size of the 304 SS steel balls from 4 to 8 mm in diameter. Figure 55, *a*–*c* shows cross-section images of the processed samples with different sizes of the balls (from 8 mm to 4 mm). As can be clearly seen, the increase in the thickness of the deformed region is observed with an increase in the size of the balls. The thickest deformed zone (42 ± 2 μm) is formed when the balls with a diameter of 8 mm are used. For the balls of 6 and 4 mm, these zones are reduced to 36 and 32 μm, respectively.

Based on the x-ray diffraction patterns, the observed peaks correspond to Fe with crystallographic planes (110), (200), and (211), at 2θ

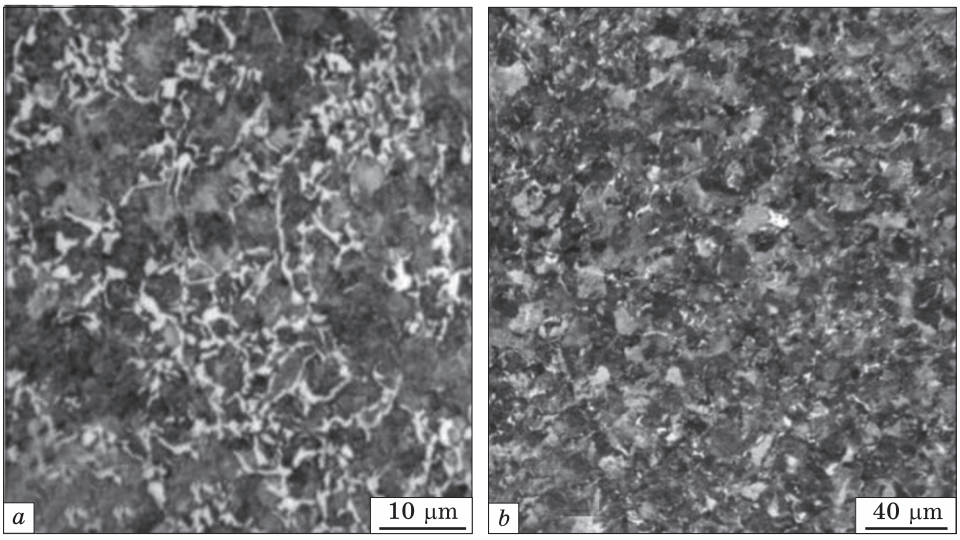

Fig. 50. Microstructure of the AISI 1050 steel: *a* — before, *b* — after accomplished heat treatment [38]

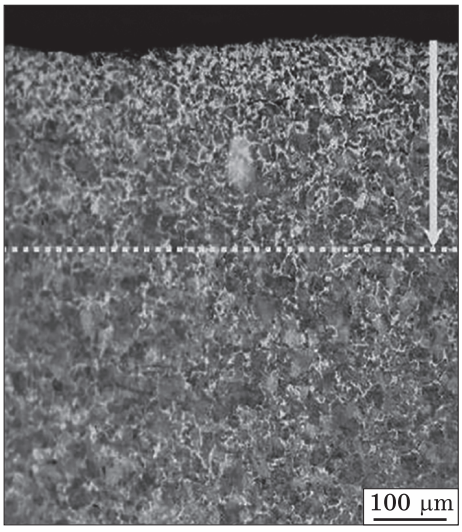

Fig. 51. Optical images of the treated specimens SOSP [38]

diffraction angles of 44.67°, 64.91°, and 82.18°, respectively, for two states of the samples. It can be noted that after SMAT processing, the peak is shifted towards the smaller angle 2θ 44.67°, as shown in Fig. 56, *b*. This fact suggests that severe deformation leads to a decrease in the value of the interplanar distance. The average grain size calculated by Scherrer's equation for processed samples is in the range of 44–55 nm.

Fig. 57 shows the dark-field TEM image of the treated surface. Few dislocation walls and dislocation loops are visible, which also appeared on the surface. After processing with 4 mm balls, highly disoriented and inhomogeneous dislocation walls were formed due to the rapid and accidental impact of the balls on the surface. This multiplication initiated the interlacing of the dislocations growing on the different slip planes in a complex manner, causing the formation of the grain subunits or the dislocation loops on the surface. The inset in Fig. 58, *a* shows the selected area

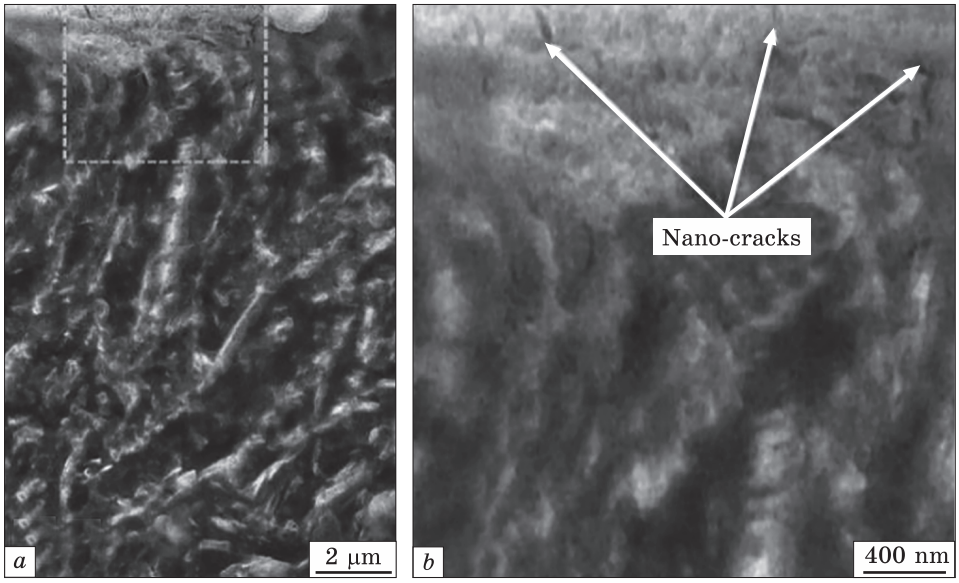

Fig. 52. SEM observations of the severely SP specimens SOSP [38]

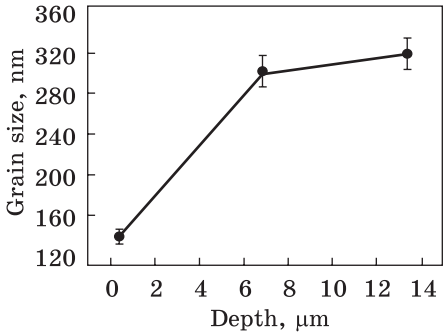

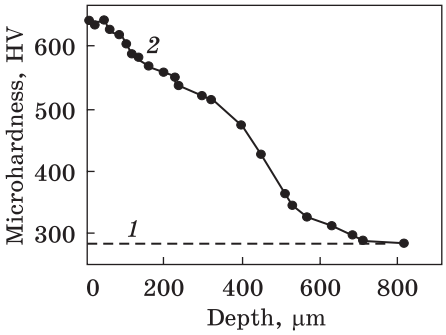

Fig. 53. The grain size variations in terms of the depth from the surface [38]

Fig. 54. Microhardness depth distribution for the SP treated sample showing decrease from the top surface to the bulk [38]

electron diffraction pattern (SAED), in which twins of the type (110), (200), and (211) are visible, corresponding to the plane of deformation as the result of the presence of the almost equiaxed nanograins with the random orientation. Figure 57, *b* shows the appearance of the deformation twins. Since AISI 1020 steel is known to have low stacking fault energy, plastic deformation by mechanical twinning is the dominant mechanism. The dislocation density measured for the untreated sample was $0.0136 \cdot 10^{19}$ m^{-2}, which gradually increased to $0.015 \times \times 10^{19}$ m^{-2} and $0.0162 \cdot 10^{19}$ m^{-2} for processing with 8 mm and 6 mm balls, respectively.

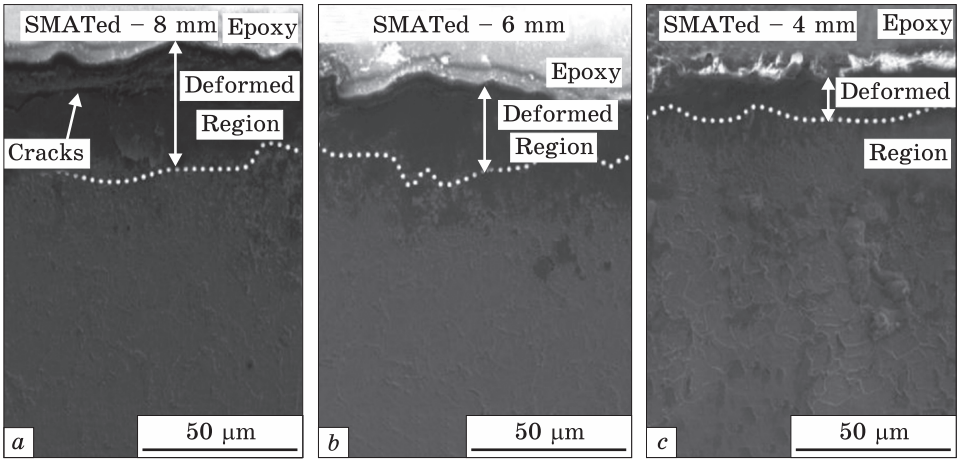

Fig. 55. Cross-sectional SEM images of SMATed LCS-steel with different ball sizes: *a* — 8 mm; *b* — 6 mm; *c* — 4 mm [39]

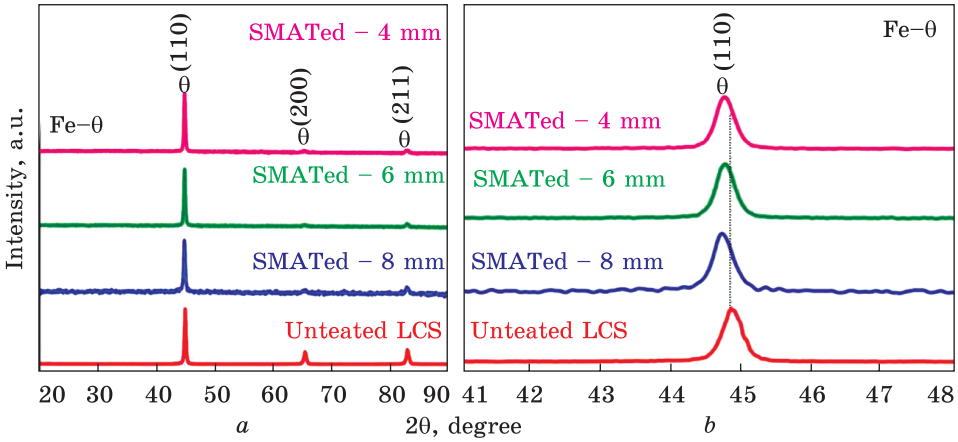

Fig. 56. XRD pattern of (*a*) untreated LCS, SMATed — 8 mm, SMATed — 6 mm and SMATed — 4 mm (*b*) shows peak broadening and shifting at 2θ angle of 44.67° [39]

The authors [40] investigated the medium-carbon steel grade AISI 1045 of the following composition (wt.%): C 0.43; Mn 0.35; Si 0.15; Cr 0.19; Mo 0.02; P 0.02; S 0.02; and balance Fe. This steel is commonly used in general engineering for the manufacture of hydraulic cylinders, shafts, and medium- to high-strength threaded connections.

The original samples (after proper grinding, polishing and ultimately etching with 4% Nital) were first preheated to 200 °C for 1 hour and then austenitized at 900 °C for 1 hour in the carbon-neutral atmosphere; then they were immediately quenched in oil and tempered at 400 °C for 1 h, followed by cooling in air. The resulting microstructure had an average hardness of 36 HRC (355 HV). Figure 58 depicts the micro-

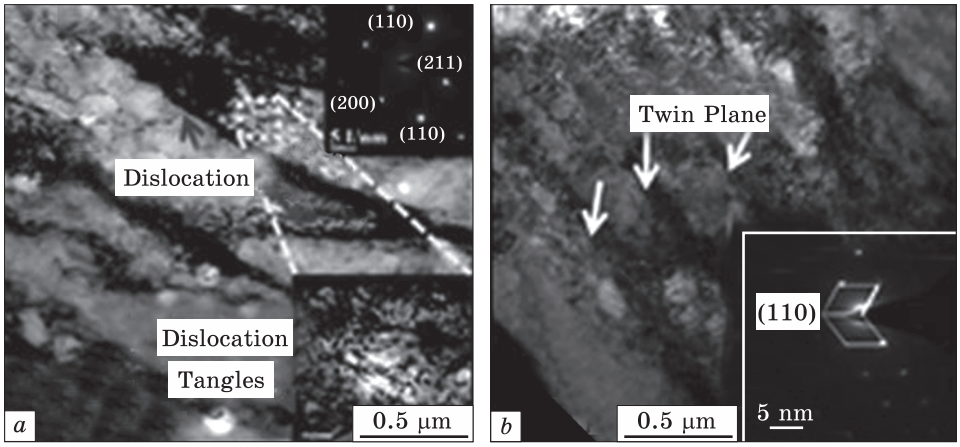

Fig. 57. a — the dark field TEM-images showing dislocation walls and tangles along with corresponding SAED pattern as inset image; *b* — the twin plane shown by arrows along with SAED pattern of (110 plane) for SMATed-4 mm [39]

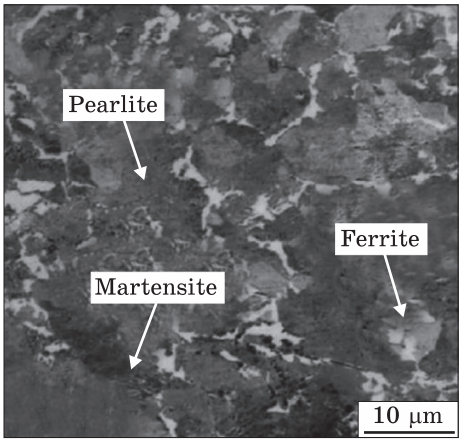

Fig. 58. Microstructure of the AISI 1045 steel after heat treatment [40]

structure of AISI 1045 after heat treatment. The material consists of the pearlite, martensite, and ferrite structures with an average grain size of 7.5 μm.

High-intensive shot penning (HISP) was carried out using standard 48–52 HRC steel balls (S230, S280, and S330) with an average diameter of 0.58 mm, 0.71 mm and 0.83 mm, respectively, at a pressure of 4– 7.5 bar and the angle of incidence of 90°. Almen intensity varied in the range of 20–32 A. Figure 60 shows the optical photomicrographs of the cross-section for all samples. Based on the observational data, the depth of

Table. 4. **Different applied HISP parameters [40]**

Treatment	Almen intensity, A	Coverage, %	Treatment	Almen intensity, A	Coverage, %
CSP	20	100	SSP4	28	2000
SSP1	22	500	OSP1	30	2500
SSP2	24	1000	OSP2	32	3000
SSP3	26	1500			

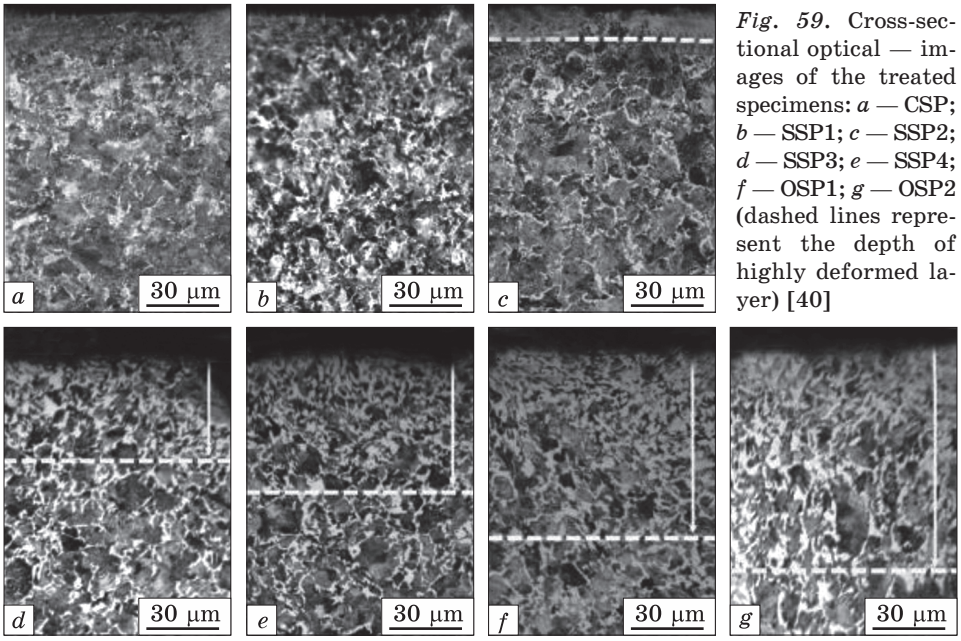

Fig. 59. Cross-sectional optical — images of the treated specimens: *a* — CSP; *b* — SSP1; *c* — SSP2; *d* — SSP3; *e* — SSP4; *f* — OSP1; *g* — OSP2 (dashed lines represent the depth of highly deformed layer) [40]

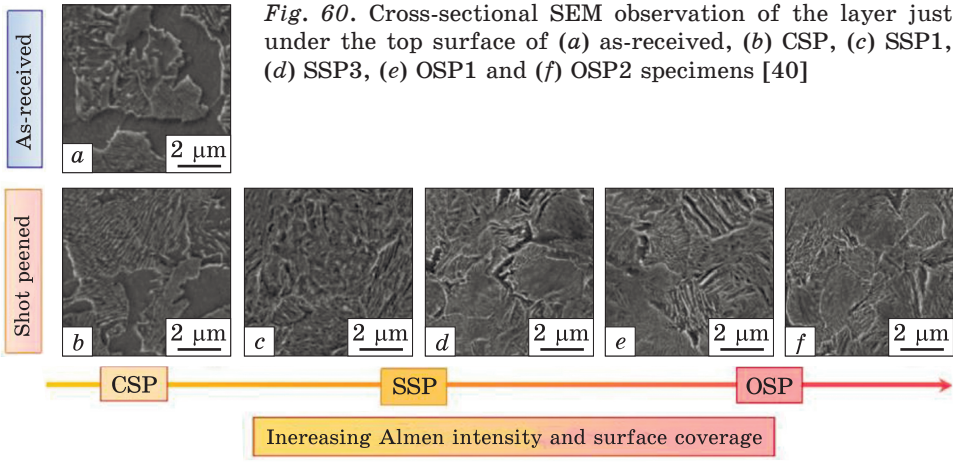

Fig. 60. Cross-sectional SEM observation of the layer just under the top surface of (*a*) as-received, (*b*) CSP, (*c*) SSP1, (*d*) SSP3, (*e*) OSP1 and (*f*) OSP2 specimens [40]

the deformed layer was 9 μm, 13 μm, 18 μm, 47 μm, 66 μm, 93 μm, and 106 μm for samples after conventional shot peening (CSP), severe shot peening (SSP) for four various coverages: SSP1, SSP2, SSP3, SSP4, and two over shot peening (OSP): OSP1, and OSP2, respectively. These depths represent the average of seven measurements at different locations for each sample. Dashed lines for each sample show the approximate boundaries of the coarse-grained zone with refined ones. Microscopic observations show that with an increase in the Almen intensity

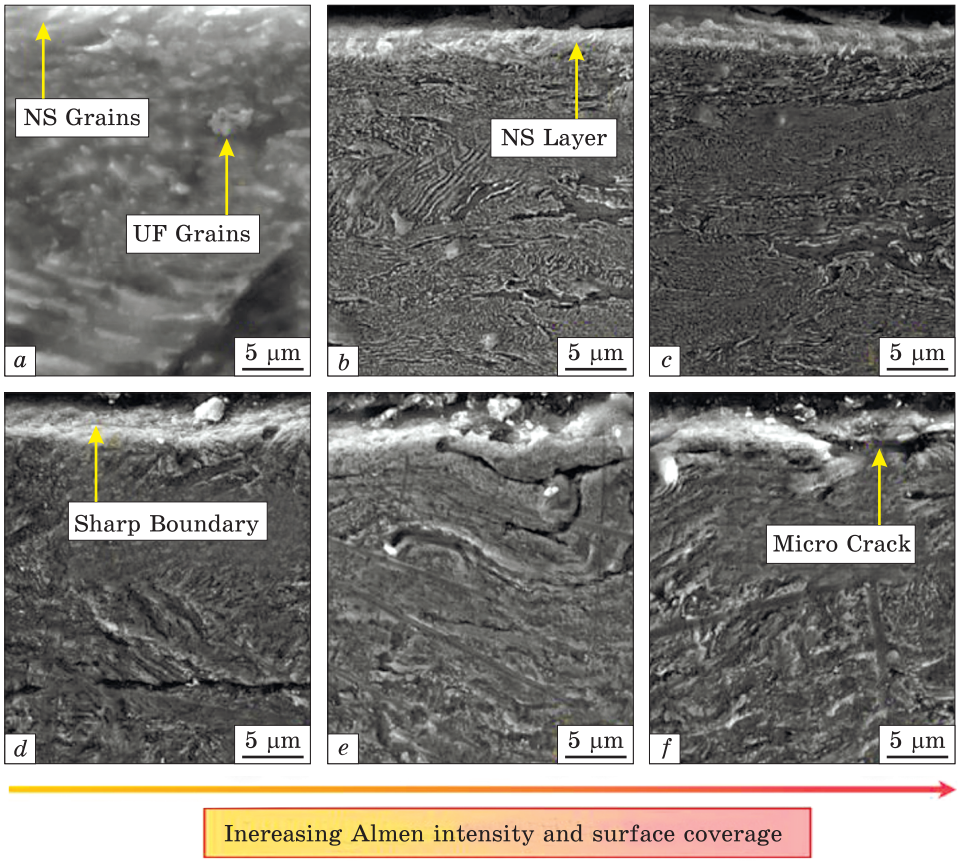

Fig. 61. Cross-sectional FESEM observations of the (*a*) SSP1, (*b*) SSP2, (*c*) SSP3, (*d*) SSP4, (*e*) OSP1 and (*f*) OSP2 specimens [40]

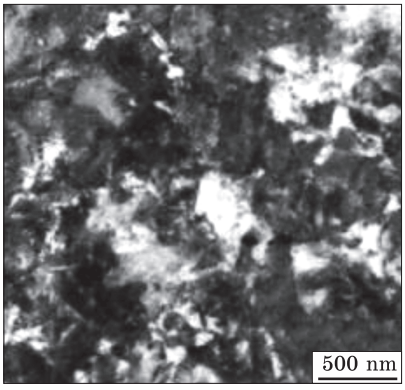

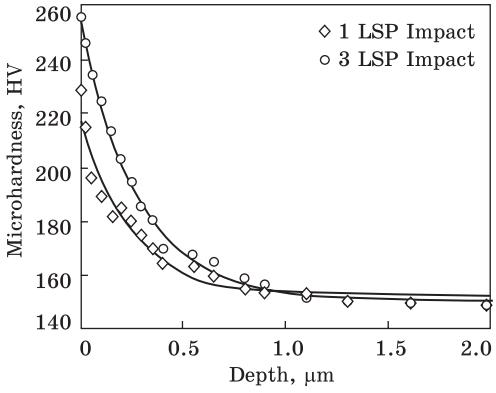

Fig. 62. Bright-field TEM image of the CSP specimen [40]

Fig. 63. Microhardness distribution AISI 8620 steel after a single LSP impact and three LSP impacts [44]

(Table 4) and the surface coverage, the depth of the deformed layers increases. SEM observations in the cross-sections of the initial and treated specimens (Fig. 60) show the higher density of the grain boundaries and the formation of the dense structure caused by the increased kinetic energy of the applied hardening treatments from CSP to OSP2. Based on the TEM observations presented in Fig. 61, high deformation and reduced grain size are clearly visible near the upper surface layer. Analysis of the broadening of x-ray diffraction peaks (200), (211), (220), and (3110) b.c.c. Fe by the Williamson–Hall method, the grain size was determined for each processing mode (Fig. 62). As can be seen from this figure, the thickness of the deformed layer is 300–650 μm. It is obvious that the growth of the microhardness depends on the intensity of processing.

4. Laser Shock Peening

Laser shock peening/processing (LSP) is an advanced technique to improve wear and corrosion resistance, as well as enhance the fatigue properties of both small-sized and large-scale metal components. During LSP treatment, SPD of the metal surface is generated by the strain induced by multiple laser shock waves. The effects of the LSP technique on the surface properties of stainless steels were mainly studied [41–43]. Compared to the conventional peening techniques, the laser shock peening process leads to deeper compressive residual stress and surface hardness distribution values in the near-surface layers of the stainless steels and carbon or alloyed steels leading to the improvement of their surface properties.

Lu *et al*. [44] studied the effect of the multiple LSP impacts with different pulse energy on structure, grain size, microhardness, and wear behaviours of AISI 8620 alloy steel of the following chemical composition (wt.%): 0.18–0.23 C, 0.15–0.35 Si, 0.70–0.90 Mn, ≤0.035 S, ≤0.035 P, 0.40–0.60 Cr, 0.40–0.70 Ni, ≤0.030 Cu, 0.15–0.25 Mo, and balance Fe. The AISI 8620 steel is used for a number of medium-strength applications, such as camshafts, fasteners, and gears.

The surface microhardness magnitudes of the LSP-processed specimens are respectively enlarged by about 47% and 60% after a single LSP impact and three LSP impacts in comparison with the unpolished/initial specimen (149 $HV_{0.2}$) (Fig. 63).

A study made by Lu [44] revealed that the average size of the original grains in the near-surface layer of the untreated specimen is in a range from 100 nm to 1 μm while the average size of the refined grains in the subsurface layer of the LSP-peened specimen is about 10 nm (Fig. 64).

In addition, they showed that the microstructural hardening mechanism of multiple LSP impacts on AISI 8620 steel is characterized by the

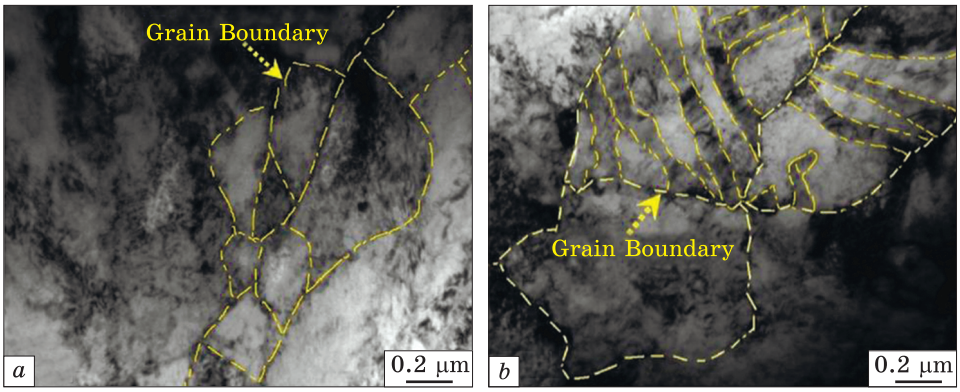

Fig. 64. TEM images of near-surface grains in the subsurface layer of the untreated specimen (*a*) and LSP-processed specimen (*b*) of AISI 8620 steel [44]

refinement of coarse grains in the near-surface region by dislocation movement and dispersion strengthening of C atoms, which cut cementite and diffused into the ferrite by moving dislocations. As a consequence, the improvement of wear resistance was observed after LSP due to the grain refinement in the surface layer of AISI 8620 steel.

The effects of the laser shock processing on the surface microstructure, nanocrystallization, hardness, and residual stress of the medium-carbon AISI 1045 steel (~0.45 C wt.%) and AISI 4140/4340 low-alloyed steels were evaluated in works [45–48]. The specimens were machined from an AISI 4140 steel plate of a chemical composition (all wt.%): 0.41 C, 0.91 Cr, 0.83 Mn, 0.21 Si, 0.025 P, 0.027 S, 0.18 Mo, the remainder Fe. The chemical composition (wt.%) of AISI 4340 alloy steel was as follows: 0.38–0.43 C, 1.65–2.0 Ni, 0.70–0.90 Cr, 0.65–0.90 Mn, 0.15–0.30 Si, 0.15–0.25 Mo, ≤0.025 P, ≤0.025 S, and balance Fe. AISI 4140 and 4340 steels are widely used in general purpose high tensile steel for components, like axles, shafts, gears, *etc*.

The initial microstructure of quenched and tempered AISI 4140 steel consisted of a retained lath-type martensite (indicated by the arrows in Fig. 65, *a*) and a low density of lath-type precipitates (Fe_3C type) (indicated by the arrows in Fig. 65, *b*). The pile-up of localized dislocations and lamellar dislocation boundaries were found (indicated by the arrows in Fig. 65, *d*, *e*). The formed dislocation bands can be observed in Fig. 66, *f* and Fig. 65 at high magnifications.

In Fig. 66, *a* and Fig. 66, *b*, *a* number of precipitates are observed near the subgrain boundaries, while few precipitates are observed within the subgrains. This is due to the high carbon atom concentration near the sub=grain boundaries. Figure 66, *c* shows a TEM image of a precipitate at higher magnification. The nanocrystalline surface (around 10 μm from the top) is presented after LSP in Fig. 66, *d*.

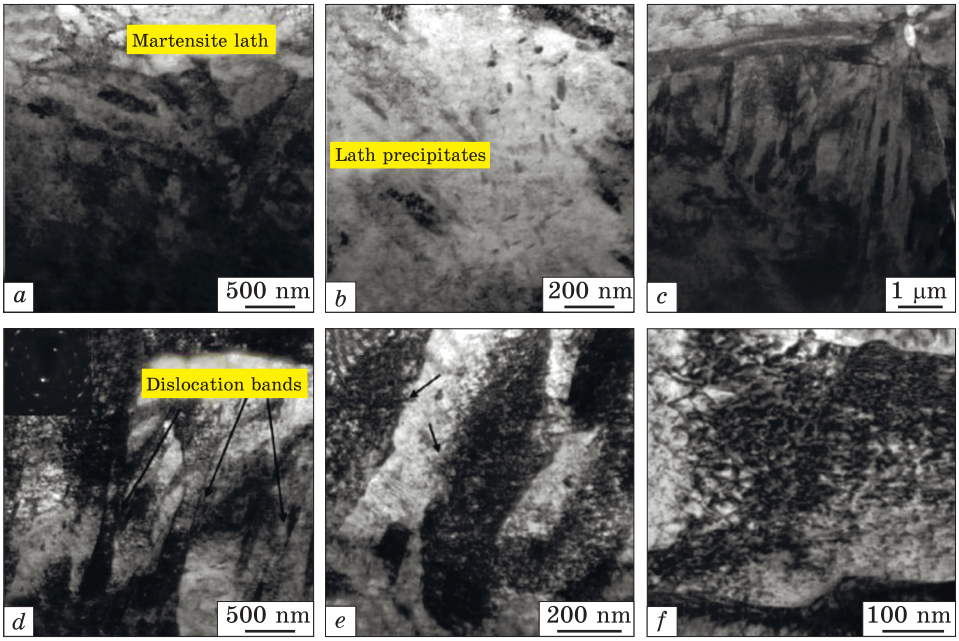

Fig. 65. TEM images of near-surface microstructure in the initial state (*a*, *b*) and LSP-processed specimens of AISI 4140 steel (*c*–*f*) in the near-surface layer at different magnifications [46]

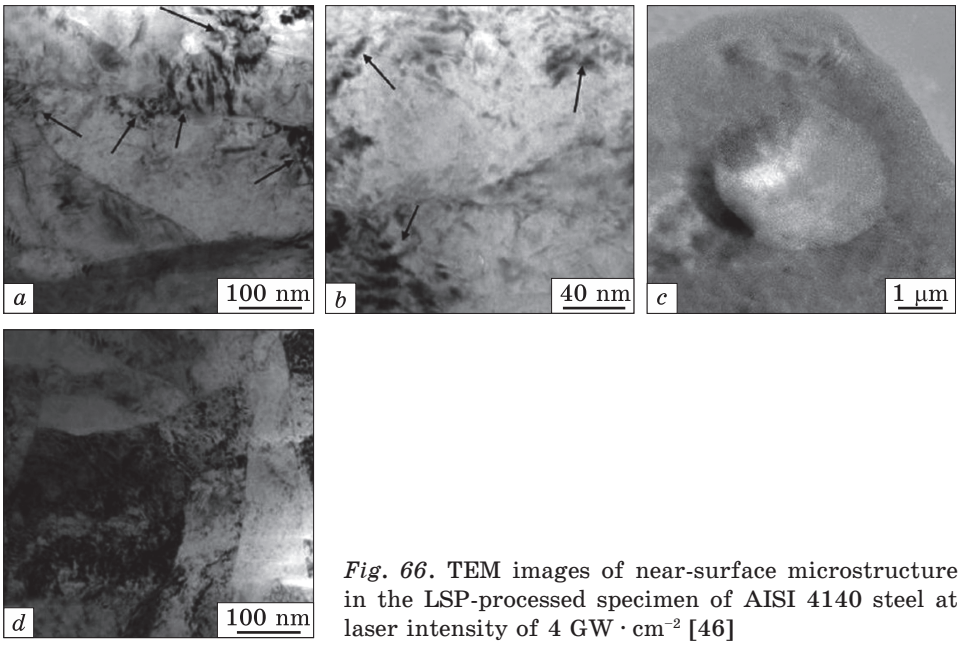

Fig. 66. TEM images of near-surface microstructure in the LSP-processed specimen of AISI 4140 steel at laser intensity of 4 GW · cm^{-2} [46]

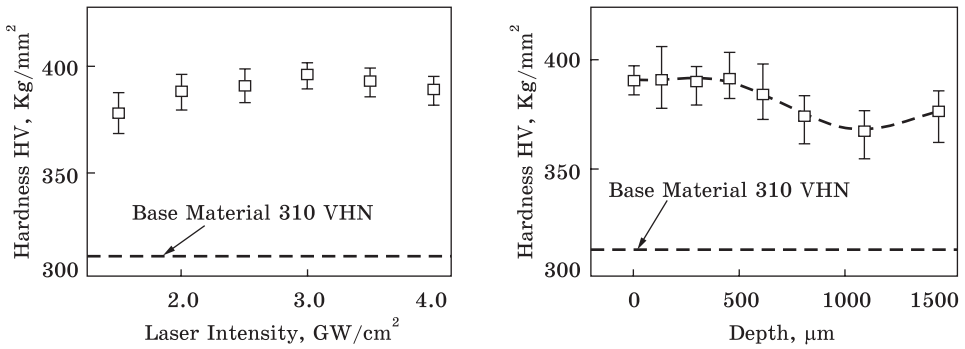

Fig. 67. Surface hardness of the LSP-processed specimens of AISI 4140 steel at different laser intensities [46]

Fig. 68. Hardness depth profile in the LSP-processed specimen of AISI 4140 steel [46]

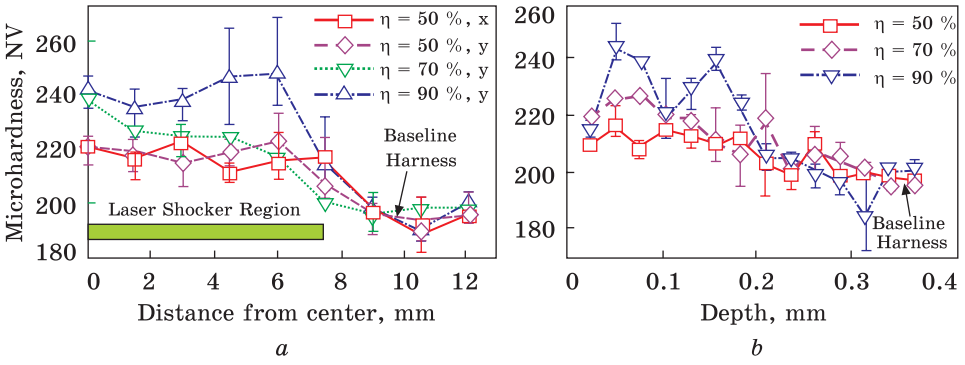

Fig. 69. Microhardness profiles on top surface (*a*) and in depth (*b*) of the LSP-processed specimen of AISI 1045 steel [45]

The surface hardness of the LSP-processed specimen of AISI 4140 steel at different laser intensities is shown in Fig. 67. It was observed that increasing the laser intensity resulted in an increase in the surface hardness.

The microhardness distribution in the near-surface layers of the LSP-processed specimen of AISI 4140 steel at laser intensity of 4 GW · cm^{-2} is given in Fig. 68. It can be seen that the surface microhardness magnitudes increase from 310 HV to 390 HV after LSP, providing the hardening depth of about 1 mm.

The profiles of the microhardness on the top surface and in depth in the multi-pin LSP-peened AISI 1045 steel are presented in Fig. 69. In general, the surface hardness slightly decreased to the untreated specimen in depth at a distance of ~0.2 mm from the top surface.

A study made by Hu [45] confirmed that a martensite transformation area was found near the top surface about 20 μm thick in the LSP-

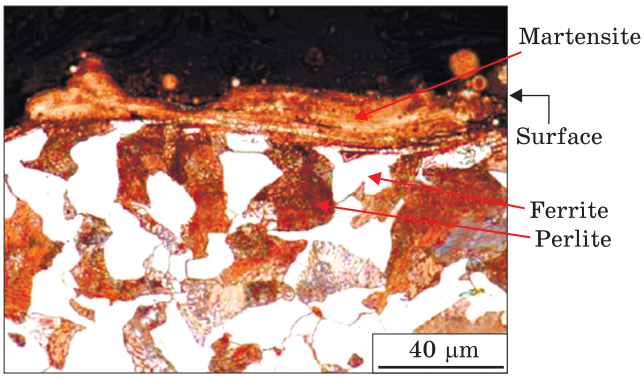

Fig. 70. Microstructure in the LSP-processed specimen of AISI 1045 steel [45]

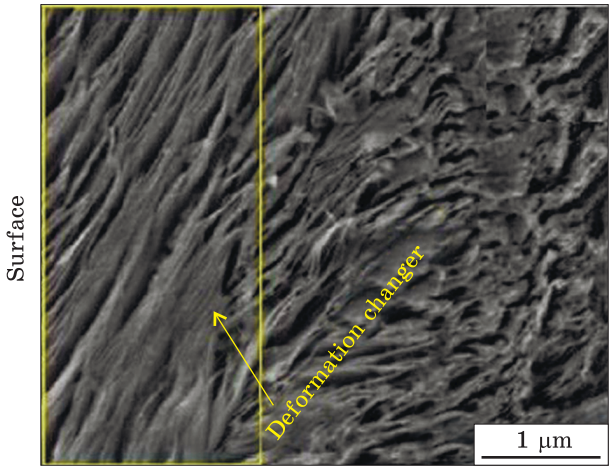

Fig. 71. SEM image of near-surface microstructural changes in the LSP-processed specimen of SAE 9254 spring steel [49]

peened specimen due to SPD. At the same time, the martensite was also observed to be plastically deformed by the impact (Fig. 71).

Works by Prabhakaran [49] and Ganesh [50] confirmed that the work hardening depth and nanomechanical properties were significantly enhanced in AISI 9254/AISI 9260 spring steel by the LSP process without a coating. They are respectively composed of (in wt.%) 0.51–0.590.56–0.64 C, 1.20–1.60/1.8–2.2 Si, 0.60–0.80/0.75–1.0 Mn, 0.60–0.80/≤0.035 Cr, ≤0.035 P, ≤0.04 S, and the base metal Iron. The above-mentioned steels are used not only for the production of the leaf and conical springs but also in many other areas as a high-strength alloy.

The grain refinement features, such as nanotwins, micro shear bands, and shear cells were revealed in the subsurface layer due to high strain-induced deformation by the LSP treatment (Fig. 71, Fig. 72).

The major plastic deformations were observed up to 10–15 μm from the surface. The needle-like bainitic structural changes on the surface are evident in the LSP-induced deformations. The presence of bainitic ferrite, retained austenite, and twin lines can be seen in Fig. 72, *a*,

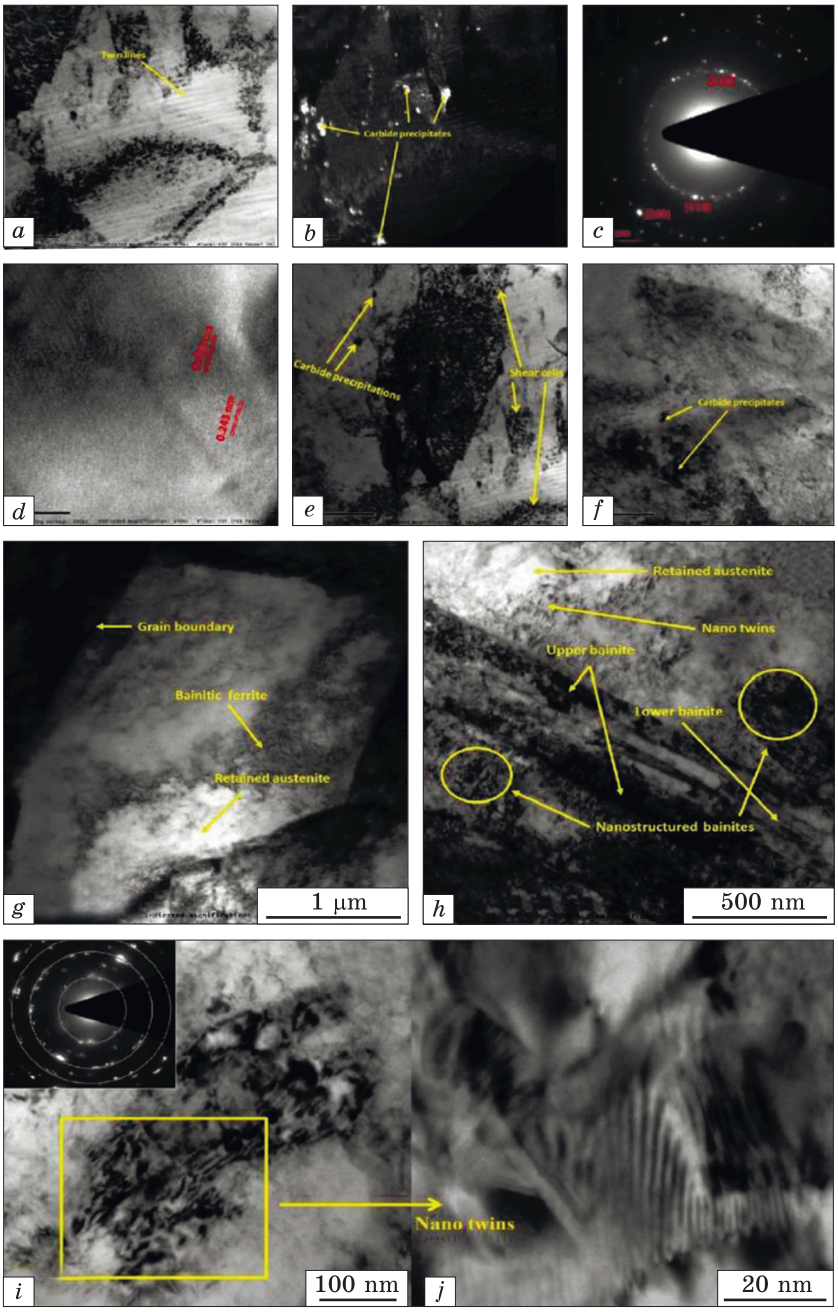

Fig. 72. TEM images of near-surface microstructure in the LSP-processed specimen of SAE 9254 spring steel [49]

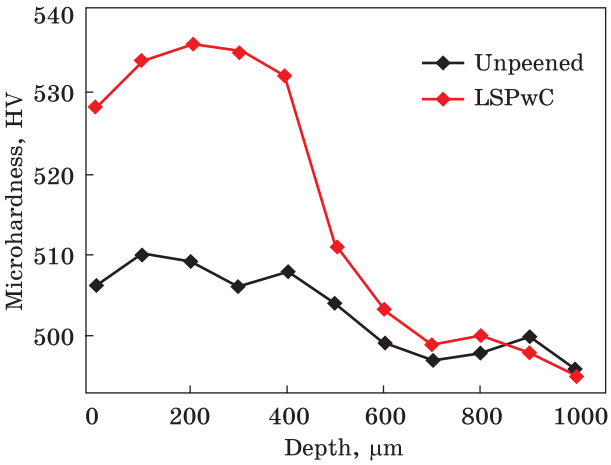

Fig. 73. Surface microhardness depth profiles of the unpeened and LSP-peened specimen of SAE 9254 spring steel [49]

Fig. 72, *e*, Fig. 72, *f*. The nanotwins' lines and nanostructured bainite can be observed in Fig. 72, *i* and Fig. 72, *h* at high magnification, respectively. Figure 72, *c* shows the presence of ferritic planes (110) and (200), and this may be another evidence for the martensite phase transformation trend taking place after LSP processing. Compared to the untreated specimen (~0.5 nm), an averaged *d*-spacing for the LSP-treated specimen was doubled (Fig. 72, *d*). The dislocations and micro shear structures/cells are presented in Fig. 73, *e*. The finer carbide precipitations were also found in the dislocation area (Fig. 72, *f*).

As a consequence, the surface hardness was increased due to the formation of the fine-grained structure (Fig. 72). The LSP-processed specimen exhibits improved near-surface hardness magnitudes up to the depth of 0.8 mm.

To enhance surface treatment process of complexly shaped steel parts, the selective LSP technique can be a successful potential replacement for a conventional shot peening in various structural engineering applications.

5. Conclusions

Currently, carbon steels are still the most important structural and tool materials for numerous applications in modern mechanical engineering. The performance of machines is directly related to the quality of the surface layer of the parts, and it largely determines their service life. Therefore, the engineering practice, particularly the engineering, automotive, and aerospace industries, can hardly be imagining without finish mechanical surface treatment processes. Today, finishing surface treatment processes are necessary in order to improve tribological properties, prevent fatigue failures and corrosive destruction of the machine components and parts made of steel. Therefore, the improvement of the surface layer properties has become a topic that has attracted consider-

able interest. Optimizing the surface microstructures and properties is currently a promising way to enhance the overall performance of the materials, including carbon steels. Given the evidence of unique properties for the bulk nanocrystalline materials, it is reasonable to produce the modified nanostructured surface layer using SPD for significant improvement in the overall properties and behaviour of the materials surface. Such surface nanocrystallization will provide a new approach to the application of nanotechnology in engineering steels. There are several variants of methods to introduce nanograins and grain size gradients into the near-surface region of bulk metals and alloys based on the principle of the surface SPD.

This review is devoted to the modern view of the nanostructuring processes of the surface layers in the low carbon steel (C 0.05–0.2%), medium carbon steel (C 0.35–0.65%) and high carbon steel (C 1.0–1.5%) under the most developed surface SPD methods of the metal surfaces in recent years: ultrasonic impact peening (UIP), high-frequency impact peening (HFIP), air blast shot peening (ABSP), surface mechanical attrition treatment (SMAT) And laser shock peening (LSP).

Before SPD, the microstructure in the bulk of the annealed ferrite-pearlite low- and medium-steel sample consists of the mixture of the structurally free polyhedral ferrite grains with a size of 5–15 microns and pearlite colonies. As the carbon content increases, the portion of the pearlite increases, and the portion of the ferrite conversely decreases. In the case of spheroidized annealing, the high-carbon steel consists of the spheroidal cementite particles ranging in size from 1 μm to 200 nm, embedded in the ferrite, the average grain size of which is 15 μm. As a rule, before SPD, carbide particles are formed in the form of microplates. After standard heat treatment, the steel structure consists of the martensite with an average grain size of 2.3 μm.

The main feature for all methods of the surface SPD is the formation of the gradient near-surface deformation zone, consisting of the following strain hardening areas: nanocrystalline area, sub-grain structure, and submicrocrystalline area. Depending on the chemical composition of the steels and SPD modes, the total thickness of the deformed zone lies in the range of 50–600 μm (according to the data of layer-by-layer microhardness measurements). Each of these areas is characterized by the different degrees of grain refinement of the phases present, as well as the density and structure of the dislocation cells.

All investigated steels and SPD methods are characterized by notable surface grain refinement. The nanocrystallization can occur within near-surface layer of a few microns thick, and below it, there is the strain hardening area. The average grain size in the top surface layer can be as small as a few nanometers and it gradually increases with a distance from the surface.

Strain-induced microstructure evolution, including grain refinement of the ferrite, pearlite grains, and cementite was examined using the x-ray analysis and transmission electron microscopy. The homogeneous layer with equiaxed grains 8–50 nm in size is visible close to the outmost surface. The thickness of the nanostructured surface layer is not less than 20 μm.

For ferrite, grain refinement includes the formation of the dense dislocation walls and dislocation clusters in the initial coarse grains, as well as in the crushed crystallites/cells (with further deformation), the transformation of these microstructures into sub-boundaries with low-angle misorientation, and the evolution of the sub-boundaries into highly misoriented grain boundaries. After severe deformation, transformation is also observed in the pearlite grains. Intensive dissolution of the pearlite plates occurs in the ferrite/pearlite colonies. This is due to the fact that severe hardening made the lamellar cementite in pearlite spheroidal with partial dissolution. According to TEM analysis, the volume fraction of the cementite significantly decreases with increasing deformation (i.e., with decreasing depth). Closer to the top surface layer electron microdiffraction does not detect the presence of cementite particles) indicating the cementite dissolution induced by increased plastic straining.

Severe plastic deformation leads also to a significant increase in the dislocation density and a slight decrease in the size and number of carbides in the microstructure of the surface layer. The density of the dislocations in the severe-deformed ferrite grains is two orders of magnitude higher than that observed in the original grains. The dislocations are known to promote the dissolution the carbon atoms into adjacent ferrite interlayers. This is due to the fact that the binding energy between the C and Fe atoms in the cementite is lower than the interaction energy between the C atom and the dislocation. Consequently, moving dislocations can capture C atoms with the decrease in the cementite size during plastic deformation and their transformation into ferrite. The presence of many dispersed cementite particles, which greatly facilitate the nucleation of the dislocations in the ferrite during deformation, contributes to the refinement of the ferrite grains. Accumulated multiple gliding progressively refines cementite into nanosize cementite particles mixed within ferrite nanograins in the top surface layer. The decreasing volume fraction of the cementite is observed with decreasing depth in the top deformed layer, indicative of dissolution of the cementite induced by increasing plastic deformation.

In conclusion, increased hardness and the deeper hardening zone can be obtained by surface SPD treatment. The maximum hardening effect is about 200%.

Acknowledgements. The paper contains results carried out within the framework of the projects of Ministry of Education and Science of Ukraine and National Academy of Sciences of Ukraine (grant numbers 0121U109752 and 0119U001167).

REFERENCES

1. D. Llewellyn, R. Hudd, *Steels: Metallurgy and Applications* (Elsevier: Butterworth-Heinemann: 1998).
2. T. Islam and H.M.M.A. Rashed, Classification and Application of Plain Carbon Steels, *Reference Module in Mater. Sci. Mater. Eng.* (Elsevier: 2019); https://doi.org/10.1016/B978-0-12-803581-8.10268-1
3. A. Rosochowski, L. Olejnik, Severe plastic deformation for grain refinement and enhancement of properties (Eds. J. Lin, D. Balint, and M. Pietrzyk), Woodhead Publishing Series in Metals and Surface Engineering, Microstructure Evolution in Metal Forming Processes (Woodhead Publishing: 2012), pp. 114–141; https://doi.org/10.1533/9780857096340.1.114.
4. R.Z. Valiev and I.V. Aleksandrov, *Nanostructured Mater.*, **12**: 35 (1999); https://doi.org/10.1016/S0965-9773(99)00061-6
5. C.E. Carlton and P.J. Ferreira, *Acta Mater.*, **55**: 3749 (2007); https://doi.org/10.1016/j.actamat.2007.02.021
6. M.A. Vasylyev, G.I. Prokopenko, and V.S. Filatova, *Usp. Fiz. Met.*, **5**, No. 3: 345 (2004) (in Ukrainian); https://doi.org/10.15407/ufm.05.03.345
7. V.E. Panin, A.V. Panin, *Physical Mezomechanics*, **8**: 7 (2005) (in Russian); https://doi.org/10.24411/1683-805X-2005-00092
8. V.P. Alekhin and O.V. Alekhin, *Deform. & Fracture Mater.*, No. 9: 32 (2008) (in Russian).
9. M.O. Vasylyev, V.K. Nosenko, I.V. Zagorulko, and S.M. Voloshko, *Prog. Phys. Met.*, **21**, No. 3: 319 (2020); https://doi.org/10.15407/ufm.21.03.319
10. C.S. Montross, T. Wei, L. Ye, G. Clark, Y.-W. Mai, *Int. J. Fatigue*, **24**: 1021 (2002); https://doi.org/10.1016/S0142-1123(02)00022-1
11. T.O. Olugbade, J. Lu, *Nano Mater. Sci.*, **2**: 3 (2020); https://doi.org/10.1016/j.nanoms.2020.04.002
12. V.A. Klimenov, O.N. Nekhoroshkov, P.V. Uvarkin, Zh.G. Kovalevskaya, and Yu.F. Ivanov, *Phys. Mesomechanics*, **9**: 173 (2006)) (in Russian); https://doi.org/10.24411/1683-805X-2006-00074
13. Ya.N. Otteniy and A.M. Lavrentiev, *Izvestiya VSTU*, **9**: 50 (2017) (in Russian).
14. C.-M. Suha, G.-H. Song, M.-S. Suh, and Y.-S. Pyoun, *Mater. Sci. Eng. A*, **443**: 101 (2007); https://doi.org/10.1016/j.msea.2006.08.066
15. W. Ting, W. Dongpo, L. Gang, G. Baoming, and S. Ningxi, *Appl. Surf. Sci.*, **255**: 1824 (2008); https://doi.org/10.1016/j.apsusc.2008.06.034
16. Z. Ren, R. Chiang, H. Qin, V.K. Vasudevan, G.L. Doll, Y. Dong, and C. Ye, *Wear*, **458-459**: 203398 (2020); https://doi.org/10.1016/j.wear.2020.203398
17. X.J. Caoa, Y.S. Pyounb, and R. Murakamia, *Appl. Surf. Sci.*, **256**: 6297 (2010); https://doi.org/10.1016/j.apsusc.2010.04.007

18. A.V. Panin, O.B. Perevalova, E.A. Sinyakova,Y.I. Pochivalov, M.V. Leontyeva-Smirnova, V.M. Chernov, V.E. Panin, *Fiz. Khim. Obrab. Mater.*, **4**: 83 (2011) (in Russian).
19. Zh.G. Kovalevskaya, Yu.F. Ivanov, O.B. Perevalova, V.A. Klimenov, and P.V. Uvarkin, *Phys. Metals Metallogr.*, **114**: 41 (2013); https://doi.org/10.1134/S0031918X12110105
20. B. Wu, J. Zhang, L. Zhang, Y.-S. Pyoun, and R. Murakami, *Appl. Surf. Sci.*, **321**: 318 (2014); https://doi.org/10.1016/j.apsusc.2014.09.068
21. W. Zhao, D. Liu, R. Chiang, H. Qin, X.H. Zhang, H. Zhang, J. Liu, Z. Ren, R. Zhang, G.L. Doll, V.K. Vasudevan, Y. Dong, and C. Ye, *J. Mater. Process. Technol.*, **285**: 116767 (2020); https://doi.org/10.1016/j.jmatprotec.2020.116767
22. B.N. Mordyuk, G.I. Prokopenko, P.Yu. Volosevych, L.E. Matokhnyuk, A.V. Byalonovich, and T.V. Popova, *Mater. Sci. Eng. A*, **659**: 119 (2016); https://doi.org/10.1016/j.msea.2016.02.036
23. D.A. Lesyk, S. Martinez, B.N.Mordyuk, V.V. Dzhemelinskyi, A. Lamikiz, G.I. Prokopenko, Yu.V. Milman, and K.E. Grinkevych, *Surf. Coat. Technol.*, **328**: 344 (2017); http://dx.doi.org/10.1016/j.surfcoat.2017.08.045
24. D.A. Lesyk, B.N. Mordyuk, S. Martinez, M.O. Iefimov, V.V. Dzhemelinskyi, and A. Lamikiz, *Surf. Coat. Technol.*, **401**: 126275 (2020); https://doi.org/10.1016/j.surfcoat.2020.126275
25. G. Liu, S.C. Wang, X.F. Lou, J. Lu, and K. Lu, *Scripta Mater.*, **44**: 1791 (2001); https://doi.org/10.1016/S1359-6462(01)00738-2
26. M. Umemoto, Y. Todaka, and K. Tsuchiya, *Mater. Trans.*, **44(7)**: 1488 (2003); https://doi.org/10.2320/matertrans.44.1488
27. Y.I. Babei, V.N. Maksimovich, Z.D. Maksimishin, L.V. Khomlyak, I.V. Gurei, T.N. Kalichak and E. N. Novosad, *Mater Sci*, **21**: 476 (1985); https://doi.org/10.1007/BF01147599
28. S. Han, S.N. Melkote, M.S. Haluska, T.R. Watkins, *Mater. Sci. Eng. A*, **488**: 195 (2008); https://doi.org/10.1016/j.msea.2007.11.081
29. H. Nykyforchyn, V. Kyryliv, O. Maksymiv, Z. Slobodyan and O. Tsyrulnyk, *Nanoscale Res. Lett.* **11**, 51 (2016); https://doi.org/10.1186/s11671-016-1266-3
30. V.G. Efremenko, Yu.G. Chabak, K. Shimizu, A.G. Lekatou, V.I. Zurnadzhy, A.E. Karantzalis, H. Halfa, V.A. Mazur and B.V. Efremenko, Mater. Design 126: 278 (2017); https://doi.org/10.1016/j.matdes.2017.04.022
31. L. Zhou, G. Liu, Z. Han, and K. Lu, *Scripta Mater.*, **58**: 445 (2008); https://doi.org/10.1016/j.scriptamat.2007.10.034
32. L. Zhou, G. Liu, X.L. Ma, and K. Lu, *Acta Mater.*, **56**: 78 (2008); https://doi.org/10.1016/j.actamat.2007.09.003
33. V.N. Gridnev and V.G. Gavriljuk, *Phys. Met.*, **4**: 74 (1982) (in Russian).
34. V.G. Gavriljuk, *Mater. Sci. Eng. A*, **345**: 81 (2003); https://doi.org/10.1016/S0921-5093(02)00358-1
35. D. Li, H.N. Chen, and H. Xu, *Appl. Surf. Sci.*, **255**: 3811 (2009); https://doi.org/10.1016/j.apsusc.2008.10.037
36. L. Zhou, G. Liu, X.L. Ma, and K. Lu, *Acta Mater.* **56**: 78 (2008); https://doi.org/10.1016/j.actamat.2007.09.003
37. W.B. Lee, K.T. Cho, K.H. Kim, K.I. Moon, and Y. Lee, *Mater. Sci. Eng. A*, **527**: 5852 (2010); https://doi.org/10.1016/j.msea.2010.05.083

38. E. Maleki, O. Unal, and K.R. Kashyzadeh, *Surf. Coat. Technol.*, **344**: 62 (2018); https://doi.org/10.1016/j.surfcoat.2018.02.081
39. S. Singh, K.K. Pandey, S.K. Bose, and A.K. Keshri, *Surf. Coat. Technol.*, **396**: 125964 (2020); https://doi.org/10.1016/j.surfcoat.2020.125964
40. E. Maleki, O. Unal, K.R. Kashyzadeh, S. Bagherifard, and M. Guagliano, *Appl. Surf. Sci. Adv.*, **4**: 100071 (2021); https://doi.org/10.1016/j.apsadv.2021.100071
41. L. Petan, J. Grum, J.A. Porro, J.L. Ocaca, and R. Šturm, *Metals* **9**: 1217 (2019); https://doi.org/10.3390/met9121271
42. D.A. Lesyk, H. Soyama, B.N. Mordyuk, V.V. Dzhemelinskyi, S. Martinez, N.I. Khripta, and A. Lamikiz, *J. Mater. Eng. Perform.*, **28**: 5307 (2019); https://doi.org/10.1007/s11665-019-04273-y
43. D. Karthik, S. Kalainathan, and S. Swaroop, *Surf. Coat. Technol.*, **278**: 138 (2015); https:// doi.org/10.1016/j.surfcoat.2015.08.012
44. J.Z. Lu, K.Y. Luo, F.Z. Dai, J.W. Zhong, L.Z. Xu, C.J. Yang, L. Zhang, Q.W. Wang, J.S. Zhong, D.K. Yang, and Y.K. Zhang, *Mater. Sci. Eng. A*, **536**: 57 (2012); https://doi.org/10.1016/j.msea.2011.12.053
45. Y. Hu and Z. Yao, *Surf. Coat. Technol.*, **202**: 1417 (2008); https://doi.org/10.1016/j.surfcoat.2007.07.008
46. C. Ye, S. Suslov, B.J. Kim, E.A. Stach, and G.J. Cheng, *Acta Mater.*, **59**: 1014 (2011); http://dx.doi.org/10.1016/j.actamat.2010.10.032
47. Y. Liao, S. Suslov, C. Ye, and G.J. Cheng, *Acta Mater.*, **60**: 4997 (2012); https:// doi.org/10.1016/j.actamat.2012.06.024
48. H. Chen, A. Feng, J. Li, T. Jia, and Y. Liu, *J. Mater. Eng. Perform*. **28**: 2522 (2019); https://doi.org/10.1007/s11665-019-04034-x
49. S. Prabhakaran, S. Kalainathan, P. Shukla, and V.K. Vasudevan, *Pre-prints*, 2018040362 (2018); https:// doi.org/10.20944/preprints201804.0362.v1
50. P. Ganesh, R. Sundar, H. Kumar, R. Kaul, K. Ranganathan, P. Hedaoo, G. Raghavendra, S. Anand Kumar, P. Tiwari, D.C. Nagpure, K.S. Bindra, L.M. Kukreja, and S.M. Oak, *Mater. Des.*, **54**: 734 (2014); http://dx.doi.org/10.1016/j.matdes.2013.08.104

Received 19.06.2021;
in final version, 11.11.2021

М.О. Васильєв[1], *Б.М. Мордюк*[2,1], *С.М. Волошко*[2], *Д.А. Лесик*[2]
[1] Інститут металофізики ім. Г.В. Курдюмова НАН України,
бульв. Академіка Вернадського, 36, 03142 Київ, Україна
[2] Національний технічний університет України
«Київський політехнічний інститут імені Ігоря Сікорського»,
просп. Перемоги, 37, 03056 Київ, Україна

ЕВОЛЮЦІЯ МІКРОСТРУКТУРИ ВУГЛЕЦЕВИХ СТАЛЕЙ ПІД ЧАС ПОВЕРХНЕВОЇ ІНТЕНСИВНОЇ ПЛАСТИЧНОЇ ДЕФОРМАЦІЇ

Огляд стосується висвітлення сучасних поглядів на еволюцію мікроструктури в конструкційних та інструментальних вуглецевих сталях під час поверхневої інтенсивної пластичної деформації (ІПД). Основну увагу приділено ефектам нанокристалізації в приповерхневій зоні низьковуглецевих сталей (С — 0,05–0,2 %), середньовуглецевих сталей (С — 0,35–0,65 %) і високовуглецевих сталей (С — 1,0–1,5 %). Розглянуто вдосконалені впродовж останніх років методи ІПД металевих поверхонь, такі як ультразвукове ударне оброблення (UIP/UIT), високочастотне ударне оброблення (HFIP), шрото-струменеве оброблення на повітрі (ABSP), механічне оброблення поверхні тертям (SMAT) і лазерне ударне оброблення (LSP). Еволюцію мікроструктури до та після ІПД вивчали за допомогою оптичної мікроскопії (ОМ), растрової електронної мікроскопії (SEM) та трансмісійної електронної мікроскопії (ТЕМ). Проаналізовано вплив параметрів ІПД на нанокристалічну модифікацію таких основних фазових компонентів вуглецевих сталей, як ферит, перліт і цементит. Представлено атомарний механізм нанокристалізації. Ефект деформаційного зміцнення, спричиненого ІПД, продемонстровано даними щодо профілів зміни мікротвердости біля поверхні.

Ключові слова: вуглецеві сталі, механічне оброблення поверхні, інтенсивна пластична деформація, мікроструктура, нанокристалізація, мікротвердість.